AGU PUBLICATIONS

JGR

Journal of Geophysical Research: Atmospheres

RESEARCH ARTICLE

10.1002/2017JD027411

Key Points:
- Decreased U.S. SO_2 emissions lead to robust surface temperature increases over most northern hemisphere land surfaces
- Temperature responses in Asia and in the United States are similar in magnitude; Arctic responses are larger
- Aerosol optical depth (AOD) response and its relationship with radiative forcing vary strongly between models

Supporting Information:
- Supporting Information S1

Correspondence to:
A. J. Conley,
aconley@ucar.edu

Citation:
Conley, A. J., Westervelt, D. M., Lamarque, J.-F., Fiore, A. M., Shindell, D., Correa, G., et al. (2018). Multimodel surface temperature responses to removal of U.S. sulfur dioxide emissions. *Journal of Geophysical Research: Atmospheres*, *123*, 2773–2796. https://doi.org/10.1002/2017JD027411

Received 6 JUL 2017
Accepted 22 FEB 2018
Accepted article online 1 MAR 2018
Published online 14 MAR 2018

Multimodel Surface Temperature Responses to Removal of U.S. Sulfur Dioxide Emissions

A. J. Conley[1], D. M. Westervelt[2,3], J.-F. Lamarque[1], A. M. Fiore[2,4], D. Shindell[5], G. Correa[2], G. Faluvegi[3,6], and L. W. Horowitz[7]

[1]ACOM Laboratory, National Center for Atmospheric Research, Boulder, CO, USA, [2]Lamont-Doherty Earth Observatory, Columbia University, Palisades, NY, USA, [3]NASA Goddard Institute for Space Studies, Columbia University, New York, NY, USA, [4]Department of Earth and Environmental Sciences, Columbia University, Palisades, NY, USA, [5]Nicholas School of the Environment, Duke University, Durham, NC, USA, [6]Center for Climate Systems Research, Columbia University, New York, NY, USA, [7]National Oceanic and Atmospheric Administration, Geophysical Fluid Dynamics Laboratory, Princeton, NJ, USA

Abstract Three Earth System models are used to derive surface temperature responses to removal of U.S. anthropogenic SO_2 emissions. Using multicentury perturbation runs with and without U.S. anthropogenic SO_2 emissions, the local and remote surface temperature changes are estimated. In spite of a temperature drift in the control and large internal variability, 200 year simulations yield statistically significant regional surface temperature responses to the removal of U.S. SO_2 emissions. Both local and remote surface temperature changes occur in all models, and the patterns of changes are similar between models for northern hemisphere land regions. We find a global average temperature sensitivity to U.S. SO_2 emissions of 0.0055 K per Tg(SO_2) per year with a range of (0.0036, 0.0078). We examine global and regional responses in SO_4 burdens, aerosol optical depths (AODs), and effective radiative forcing (ERF). While changes in AOD and ERF are concentrated near the source region (United States), the temperature response is spread over the northern hemisphere with amplification of the temperature increase toward the Arctic. In all models, we find a significant response of dust concentrations, which affects the AOD but has no obvious effect on surface temperature. Temperature sensitivity to the ERF of U.S. SO_2 emissions is found to differ from the models' sensitivity to radiative forcing of doubled CO_2.

Plain Language Summary We find that U.S. sulfur dioxide emissions influence temperatures in both the United States and in remote regions of the world. Three diverse climate models, all of which include the interaction of chemistry with the Earth system, produce similar northern hemisphere temperature responses. This is important because, while the emissions, atmospheric composition, and radiative forcing are most clearly expressed in the United States, the temperature changes are present over most of the northern hemisphere and strongest in the Arctic.

1. Introduction

Since the beginnings of the industrial revolution when scientists such as Angus Smith started documenting the local effects of industrial pollution on the British midlands (Smith, 1872), anthropogenic emissions have increased dramatically. Scientific studies have advanced our understanding of not only the atmospheric chemistry but also the global, local, and remote effects of anthropogenic emissions such as SO_2 (e.g., Boucher et al., 2013). Due to concerns with ozone, particulate matter, acid rain, health, and visibility, actions such as the Clean Air Act of 1970 in the United States have led to comprehensive federal and state regulations to limit emissions from both stationary (industrial) sources and mobile sources. In particular, such regulations led to a significant decrease in SO_2 emissions from the United States and Europe in the latter part of the twentieth century (Hoesly et al., 2017; Lamarque et al., 2010; Smith et al., 2011). More specifically, SO_2 emissions in those regions have fallen as a result of improved energy efficiency, shifts in fuel mixes, and the application of end-of-pipe desulfurization in the power sector. During the last few decades, other regions such as China have seen commensurate increases in their SO_2 emissions. Understanding the global, local, and remote impacts of regional emission changes could assist in mitigation of and adaptation to impacts and inform the attribution of recent climate trends (Bollasina et al., 2011; Booth et al., 2012).

As reported by Myhre et al. (2013), the radiative forcing of well-mixed greenhouse gases in 2011 relative to 1750 is in the range (2.22 to 3.78) W m^{-2}. Over the same period, the total radiative forcing of aerosols

(including aerosol-cloud interactions) is in the range (−1.9 to −0.1) W m^{-2}. The aerosol radiative forcing contributes the greatest portion of the total forcing uncertainty, and most of the uncertainty within aerosol forcing is in the interaction of clouds with aerosols (e. g., Myhre et al., 2013).

In this paper we examine local and remote forcings, aerosol burdens, and surface temperature responses to reductions in U.S. SO_2 emissions. Leibensperger et al. (2012) evaluated remote impacts of U.S. anthropogenic aerosols in a model using a slab ocean model with fixed ocean heat fluxes and prognosed sea surface temperatures (SSTs) as well as prescribed aerosol concentrations and cloud number concentrations, which does not allow for climate feedback on aerosol concentrations. The remote climate impact of regional aerosol emissions was highlighted by Shindell and Faluvegi (2009). In that study, the remote climate responses to forcing were found to depend on the latitude of the forcing, with even the sign of the response depending on the region of forcing. Our study is a natural extension of those studies, intended to identify the full geographical temperature response resulting from regional (instead of latitudinal bands) emission reductions. Kasoar et al. (2016) perform a similar study for SO_2 emissions from China. They find that aerosol optical depth (AOD) response to SO_2 emissions in China in the Hadley Centre Global. Environment Model 3-Global Atmosphere 4.0 (HadGEM3-GA4), Community Earth System Model version 1 (CESM1), and Goddard Institute for Space Studies ModelE2 (GISS ModelE2) models vary by a factor of 6 with the HadGEM3-GA4 having the strongest response and GISS having the weakest response. We study not only the remote temperature responses but also responses in dust and other aerosol burdens as well.

To evaluate the impacts of U.S. SO_2 emissions, we evaluate the climate responses from pairs (perturbation and control) of 200 year (or more) present-day simulations, which are identical except for the removal of anthropogenic U.S. emission of SO_2 in the perturbation simulation. We analyze results from the CESM1-Community Atmosphere Model version 5 (CAM5), Geophysical Fluid Dynamics Laboratory Climate Model version 3 (GFDL-CM3), and GISS-E2 Earth System Models (ESMs), each of which couple chemistry and climate and were recently used in the Coupled Model Intercomparison Project Phase 5 (CMIP5). We say a result is robust if the responses in all three models are similar (i.e., their confidence ranges somewhat overlap). We focus our analysis on responses in annual-mean SO_4 burden, effective radiative forcing (ERF), AOD, dust burden, and surface temperature. In an earlier paper, Westervelt et al. (2017) discussed precipitation responses in these same simulations.

An additional approach to elucidating the effects of anthropogenic aerosols on remote climate has been explored by imposing a specified aerosol across models (Voigt et al., 2017). That approach removes the complexities associated with differing aerosol formation due to transport, chemistry, photolysis, and aerosol representation, but does allow for the interaction of the heating with dynamics nor the interaction with cloud droplet formation or wet removal.

Our study, in contrast, includes the effects of differing aerosol representations, as well as varying chemistry and transport. While the magnitude of local effects on heating varies among the models, there is a generally similar pattern of forcing, leading to some confidence in the ability to compare temperature responses between models even with these additional complexities. We are also able to see some indications of feedback and responses in other aerosols with this study. We are also interested in aspects of wet and dry removal and the indirect effects in clouds, although those aspects are not extensively evaluated in this paper.

This paper is organized as follows: in section 2, we describe the three models used to perform the simulations, along with the specific experiments. In particular, we use a combination of fully coupled (atmosphere/land/ocean/sea-ice [SIC]/chemistry) simulations to evaluate the climate response to U.S. SO_2 emissions. We also use specified SST and SIC distributions (following the standard Atmospheric Model Intercomparison Project configuration; Eyring et al., 2016) in simulations to compute the ERF (see Myhre et al., 2013, for a complete definition) of U.S. SO_2 anthropogenic emissions. Section 3 describes the sulfate aerosol response associated with the removal of the U.S. SO_2 emissions; for convenience, in the rest of the paper, we will use SO_4 to refer to sulfate aerosols. Section 4 describes the AOD response. Section 5 focuses on the analysis of ERF, and Section 6 focuses on surface temperature response to such removal. Conclusions are drawn in Section 7.

Table 1
Model Simulations and U.S. Anthropogenic SO_2 Emissions Perturbations

Model	Spin up length (years)	Number of climate-perturbation comparison years	Emission year	Emission perturbation
NCAR-CESM1	107	270	2005	14.0 Tg SO_2 $year^{-1}$
GFDL-CM3	109	240	2000	14.8 Tg SO_2 $year^{-1}$
GISS-E2-R	100	200	2000	14.4 Tg SO_2 $year^{-1}$ plus 0.6 Tg SO_4 $year^{-1}$ direct emissions of SO_4

Note. For each model, both the control and perturbation simulations are initialized to the end of the spin-up run.

2. Model and Experiment Descriptions

We use three coupled atmosphere-ocean-land-SIC Earth system models, including interactive chemistry: CESM1, GFDL-CM3, and Goddard Institute for Space Studies ModelE2 (GISS-E2-R) (see Table 1). All of these models couple aerosol and precursor emissions to climate forcing and climate response interactively, in contrast to other climate models that specify aerosol distributions as a climatology. Each of these models participated in the CMIP5, which contributed to the Fifth Assessment Report of the Intergovernmental Panel on Climate Change (IPCC) (Flato et al., 2013). The versions of each of the models used here are essentially the CMIP5 versions. A brief description of model features as well as experimental setup follows.

2.1. CESM1

CESM version 1 includes the CAM5 atmospheric component. It uses a finite-volume dynamical core on a Cartesian grid at 1.875° latitude by 2.5° longitude and 30 vertical layers extending up to 2 hPa. Emissions of SO_2, black carbon (BC), and organic matter (OM) are based on Representative Concentration Pathway 6.0 for the year 2005 (Masui et al., 2011). Greenhouse gas surface concentrations are specified following Meinshausen et al. (2011). Natural emissions of volcanic SO_2 and dimethyl sulfide (DMS) are prescribed from the AEROCOM project (Dentener et al., 2006). Sulfur dioxide (SO_2) is oxidized by the hydroxyl radical (OH), hydrogen peroxide (H_2O_2), and ozone (O_3) to form sulfate (SO_4), and DMS is oxidized by both OH and the nitrate radical (NO_3) to form SO_2. Aerosol size distributions and composition are prognosed using the Modal Aerosol Model (MAM-3). The MAM-3 model includes three lognormal modes: Aitken, accumulation, and coarse (Liu et al., 2012). SO_4 mass is prognosed as a component in each of the three aerosol modes, soil dust is predicted in the accumulation and coarse aerosol modes, while BC and OM are predicted in the accumulation mode. Nitrate does not contribute to aerosols. Most of the SO_4 mass (~90%) is in the accumulation mode (Ghan et al., 2012). Each mode prognoses effective size, particle number, and speciated mass concentrations. This aerosol model includes microphysical processes such as new particle formation, coagulation, and condensation. Activation of aerosols into cloud droplets is based on the scheme of Abdul-Razzak and Ghan (2000). Aerosols affect deep convection only through direct radiative effect and not through cloud microphysics. The stratiform cloud microphysics are parameterized using a two-moment size distribution described in Morrison and Gettelman (2008) and include aerosol activation of cloud droplets based on subgrid vertical velocity. Additional details on aspects of CESM1 and CAM5 can be found in Neale et al. (2012). This is the version of CESM1 that was used in the Last Millenium Ensemble (Otto-Bliesner et al., 2016). A more complete description of the interactive chemistry can be found in Tilmes et al. (2015).

2.2. GFDL-CM3

The GFDL-CM3 model uses a finite-volume cubed-sphere horizontal grid consisting of six faces of 48 grid cells along each edge (C48), resulting in roughly a 200 km by 200 km spatial resolution. The vertical grid has 48 levels from the surface to about 0.01 hPa. Anthropogenic and biomass burning emissions of sulfur dioxide (SO_2), BC, and primary OM for 2000 are taken from Lamarque et al. (2010). Natural emissions of soil NO_x, lightning NO_x, dust, and marine emissions (organic aerosol, DMS, and sea salt) are described by Naik et al. (2013); isoprene emissions are described by Rasmussen et al. (2012). Lightning NO_x, dust, isoprene, and marine

Table 2
Model Aerosol Characteristics

Model	Aerosol size distribution	SO_4 aerosol mixing (optics)	Aerosol indirect effects	Model reference
NCAR-CESM1	Prognostic	Internal in all three modes	First, second	Neale et al. (2012)
GFDL-CM3	Prescribed	Internal (sulfate with hydrophilic black carbon, for radiation only)	First, second	Donner et al. (2011); Naik et al. (2013)
GISS-E2-R	Prescribed	External	First	Schmidt et al. (2014)

Note. First indirect effect is the aerosol effect on cloud albedo. Second indirect effect is the aerosol effect on cloud lifetime.

emissions respond to meteorology. Photolysis rates are calculated with the Fast-JX v7.1 as implemented by Li et al. (2016) Concentrations of long-lived greenhouse gases are based on Meinshausen et al. (2011). Tropospheric chemistry for aerosols and gas-phase species follows the work of Horowitz et al. (2003) and Horowitz (2006). SO_4 is formed via oxidation of SO_2 by the hydroxyl radical (OH) in the gas phase, and ozone (O_3) and hydrogen peroxide (H_2O_2) in clouds. DMS is oxidized to SO_2 by reaction with OH and nitrate radical (NO_3). Fixed lognormal size distributions are assumed for each of the externally mixed OM, BC, and SO_4 aerosols. The shortwave and longwave radiation algorithms follow Freidenreich and Ramaswamy (1999) and Schwarzkopf and Ramaswamy (1999), respectively, with updates as described in Anderson et al. (2004). Sulfate (assumed to be present as ammonium sulfate) and hydrophilic BC aerosols are internally mixed for radiation. The AOD of the internal mixture is attributed to species by mass fraction. Aerosol activation into cloud droplets is parameterized according to Ming et al. (2006), which relates the aerosol size distribution, chemical composition, and updraft velocity to cloud droplet number concentrations. Aerosols in GFDL-CM3 do not exert a microphysical effect on deep convective clouds; however, they can alter deep convection and associated precipitation through the direct effect. Aerosols influence cloud droplet formation and number density in shallow cumulus clouds, which are parameterized according to Bretherton et al. (2004). Additional details on the standard model configuration and performance can be found in Donner et al. (2011) and Naik et al. (2013).

2.3. GISS-E2-R

The version employed here, GISS-E2-R ("Russell ocean"), uses a Cartesian grid at 2° by 2.5° latitude by longitude. The dynamical core uses the linear upstream, modified "C grid" scheme based on Russell et al. (1995). The vertical grid consists of 40 layers extending up to 0.1 hPa. Emissions of SO_2, NH_3, NO_x, BC, and OM are based on Lamarque et al. (2010) for the year 2000, as in GFDL-CM3. Well-mixed greenhouse gases are prescribed as in Miller et al. (2014). Both OH and H_2O_2 oxidize sulfur dioxide and DMS in the model. The chemical mechanism is described by Shindell, Pechony, et al. (2013). In GISS-E2-R, aerosols include nitrate, SO_4, BC, and OM (primary and secondary) and are interactive with the radiation and cloud activation schemes. The aerosol size distribution is prescribed as a lognormal distribution for each of the externally mixed species, similar to GFDL-CM3. Prognostic treatment of aerosol number and mass size distributions are available in GISS-E2-R but were not used for the present study. The prognostic cloud droplet number concentration calculation follows the scheme presented in Morrison and Gettelman (2008), with aerosol activation discussed in detail in Menon et al. (2010). As in the other two models, aerosols affect deep convection only through the direct effect and not through cloud microphysics. Cloud processes are as described in Schmidt et al. (2006) and Schmidt et al. (2014). Unlike both National Center for Atmospheric Research (NCAR)-CESM1 and GFDL-CM3, GISS-E2 did not include a parameterized aerosol-cloud lifetime effect in these simulations (cf. Malavelle et al., 2017). The model version used here includes an improved treatment of nitrate aerosol that appears to correct a high bias in the previous version (Shindell, Pechony, et al., 2013).

2.4. Coupled Climate Simulations and Perturbations

Table 2 lists details of the simulation length and emissions perturbation for each of the models. NCAR-CESM1 simulation uses year 2005 emissions, whereas the GFDL-CM3 and GISS-E2 simulations use year 2000 emissions (due to a miscommunication in experimental design). CESM, as a result, has a 0.8 Tg SO_2 $year^{-1}$ smaller emissions of U.S. SO_2 in the control simulations compared to the GFDL and GISS models, which is small (about 5%) compared to the total U.S. SO_2 emissions of about 14 Tg SO_2 $year^{-1}$. For all models, the initial condition

for both the control and perturbation runs is obtained after approximately 100 years of spin up with the reference year (2000 or 2005) emissions. The control and perturbed simulations in each model use identical initial conditions, boundary conditions, and emissions, except that the perturbed simulation removes anthropogenic U.S. SO_2 emissions. Control and perturbed simulations branch from the identical spun-up state.

2.5. Statistical Analysis

Control simulations show a drift in global-average surface temperatures of comparable size to the variance in the models as can be seen in the supporting information Figure S2. As a result, a simple Student's *t* test shows limited power in measuring statistical significance of differences (perturbation distribution versus control distribution) as it includes the drift as part of the variance. We instead use a paired-sample test where the pairs are cotemporal samples of the perturbation and control; that is, we perform statistical analysis on the time series of cotemporal differences (perturbation *minus* control). We exclude the first 20 years of data to allow for some rapid adjustments in the perturbation case due to the U.S. SO_2 forcing.

Statistical analysis of time series requires careful consideration of the number of independent samples as discussed in the supporting information section S3 (Crawford & Howell, 1998; Jones, 1975; Zwiers & von Storch, 1995). For each time series (cotemporal differences of global, regional, and model-grid-point time series), we compute an effective sample size to account for autocorrelation. In the case of CESM (simulations with the strongest autocorrelation), the 240 years of data yields only 120 independent samples over some tropical ocean regions (Figure S5); however, the number of effective samples is dependent on the variable of interest, the region of interest, and the model. Confidence intervals discussed below are computed using the effective sample size.

All results in this paper are shown as the mean difference between perturbation and control plus or minus 1 standard error. Significance in maps is shown when the mean value of the change is larger than 2 standard errors (i.e., a *z*-score indicating 95% confidence). The bar and whisker plots show the mean, 1 standard error, and 2 standard error confidence intervals.

In the supporting information section S3, we review the use of standard error and the connection between standard error and significance testing. We review our use of *z*-scores and how we compute the effective sample size for a time series. We also review our use of more complex statistical models in section S4 and the reason we choose a one-step autoregressive model for this work (Akaike, 1974). We also briefly review in section S5 how model diversity provides increased confidence in multimodel averages (Knutti et al., 2017; Tebaldi & Knutti, 2007). In section S6 we describe an unsuccessful attempt to use empirical orthogonal functions to increase confidence in estimated means and standard errors (Bretherton et al., 1992; Preisendorfer & Mobley, 1988). In section S7, we use regression to evaluate the contributions of burden change to AOD change in two of the three models. And lastly, in section S8 we attempt to discover the causes of increased sulfate burdens in remote regions of one of the models.

2.6. Regional Definitions

Since variance for individual model grid points is expected to be larger than for regional averages, we might expect to obtain more statistical significance in our analysis of regional-average data. We analyze specific results in local regions: South Australia, North Australia, Central America, Western North America, Central North America, Eastern North America, Alaska, the Mediterranean Basin, Northern Europe, Southern Asia, Central Asia, Northern Asia, the Sahel, the Arctic region north of 60°N, and the Nino3.4 regions, following Stott et al. (2010) and Christidis et al. (2012). These regions are delineated in the supporting information section S1. We will refer to the Western North America, Central North America, and Eastern North America regions as being local to the emission change and all other regions as being remote from the emission change.

2.7. Radiative Forcing Simulations

As discussed in Myhre et al. (2013) and references therein, ERF is defined as the change in net top-of-atmosphere net (SW + LW) flux between the control and perturbed simulations, using specified SSTs. ERF is a better measure of the long-term climate forcing than either instantaneous radiative forcing or stratospheric-adjusted radiative forcing since rapid responses of the atmosphere and land are taken into account in the calculation.

Table 3
Global-average Values From Earth System Model Simulations

Average values	CESM	GFDL	GISS
Burden (Tg SO_4)	1.34	1.67	0.987
Lifetime SO_4 (Days)	6.1	7.9	3.3
Responses			
Δ Burden (Tg SO_4)	−0.090 ± 0.001	−0.057 ± 0.003	−0.052 ± 0.001
% Burden change	−6.7	−3.4	−5.2
Δ AOD (10^{-3})	−1.5 ± 0.2	−3.8 ± 0.3	−3.4 ± 0.4
Δ AOD_Dust (10^{-3})	−0.5 ± 0.2	−0.12 ± 0.07	−0.05 ± 0.02
Δ *T* (K)	0.071 ± 0.023	0.116 ± 0.017	0.052 ± 0.015
Sensitivities			
Δ SO_4/Δ Emission (Tg SO_4 [Tg SO_2 $year^{-1}$]$^{-1}$)	0.0064 ± 0.0001	0.0039 ± 0.0002	0.0036 ± 0.0001
Δ AOD/Δ SO_4 (Tg SO_4)$^{-1}$	0.016 ± 0.002	0.067 ± 0.006	0.065 ± 0.007
Δ *T*/Δ Burden (K (Tg SO_4)$^{-1}$)	−0.79 ± 0.26	−2.03 ± .32	−1.0 ± .3
Δ *T*/Δ AOD (K AOD^{-1})	−47. ± 24.	−31. ± 5.	−15. ± 7.
Δ *T*/Δ Emission(K (Tg SO_2 $year^{-1}$)$^{-1}$)	−0.0051 ± 0.0017	−0.0078 ± 0.0011	−0.0036 ± 0.0010

Note. Global averages, responses, and sensitivities to setting U.S. SO_2 emissions to zero. In the GISS model, the column burden of SO_4 does not include SO_4 that is condensed on dust.

The method used in this study is the fixed-SST method in which ERF is computed from simulations with SO_2 emissions identical to the control and test simulations described above, but only use the atmosphere and land components of the ESMs instead of being coupled to their respective ocean/SIC models. This is done by specifying SST and SIC distributions, following the standard Atmospheric Model Intercomparison Project configuration (Eyring et al., 2016), with the exception that we use climatological rather than historical SSTs. We use identical initial conditions for control and perturbed simulations. We do not correct the computed ERF to adjust for the land surface temperature change.

We further clarify that we do not use the regression-based method (Gregory et al., 2004), since the magnitude of the top-of-atmosphere flux changes and surface temperature changes are small compared to the variance of these quantities in the fully coupled system.

In short, we use a standard definition of ERF applied to changes in emissions, rather than changes in burdens, in order to include fully the atmospheric and land responses and feedback from the change in SO_2 emissions.

The CESM ERF is computed using 50 years of simulated data, GFDL simulated 41 years, and GISS simulated 163 years. The first five years of each run are excluded from the analysis to allow for rapid adjustments in the land and atmosphere. As will be seen later, for this small forcing, there is considerable noise in these results. Additional simulation years in the GISS model allow detection of the small forcing and regional dependence in that model.

3. Sulfate Impact From the Removal of U.S. SO_2 Emissions

The three models, CESM, GFDL, and GISS, have global SO_4 burdens of 1.34, 1.67, and 0.99 Tg SO_4, respectively (Table 3). The reported GISS model burden excludes the SO_4 coatings on dust, so its full burden is slightly larger than that listed. The global burdens correspond to SO_4 lifetimes of 6.1, 7.9, and 3.3 days in each model, respectively. The removal of U.S. SO_2 emissions in the perturbed experiment of each model leads to a global burden decrease of 0.090, 0.057, and 0.052 Tg SO_4, respectively. However, examination of the global SO_4 burden change masks important regional variations. As seen in Figure 1, the SO_4 burden change is largest in all three models over the eastern United States and Atlantic Ocean, but the magnitude of that change, as well as the global distribution of changes, varies between models.

In this experiment, the SO_4 column burden change (Figure 2) over Western North America ranges from about 0.5 to 1.0 mg m^{-2} across the models. Over Central and Eastern North America these models have burden changes of 2.0 to 4.5 mg m^{-2}. For comparison, the HTAP2 multimodel study using chemical-transport models (Stjern et al., 2016) found that the total SO_4 burden over the North American region was 3.55 ± 1.28 mg m^{-2}.

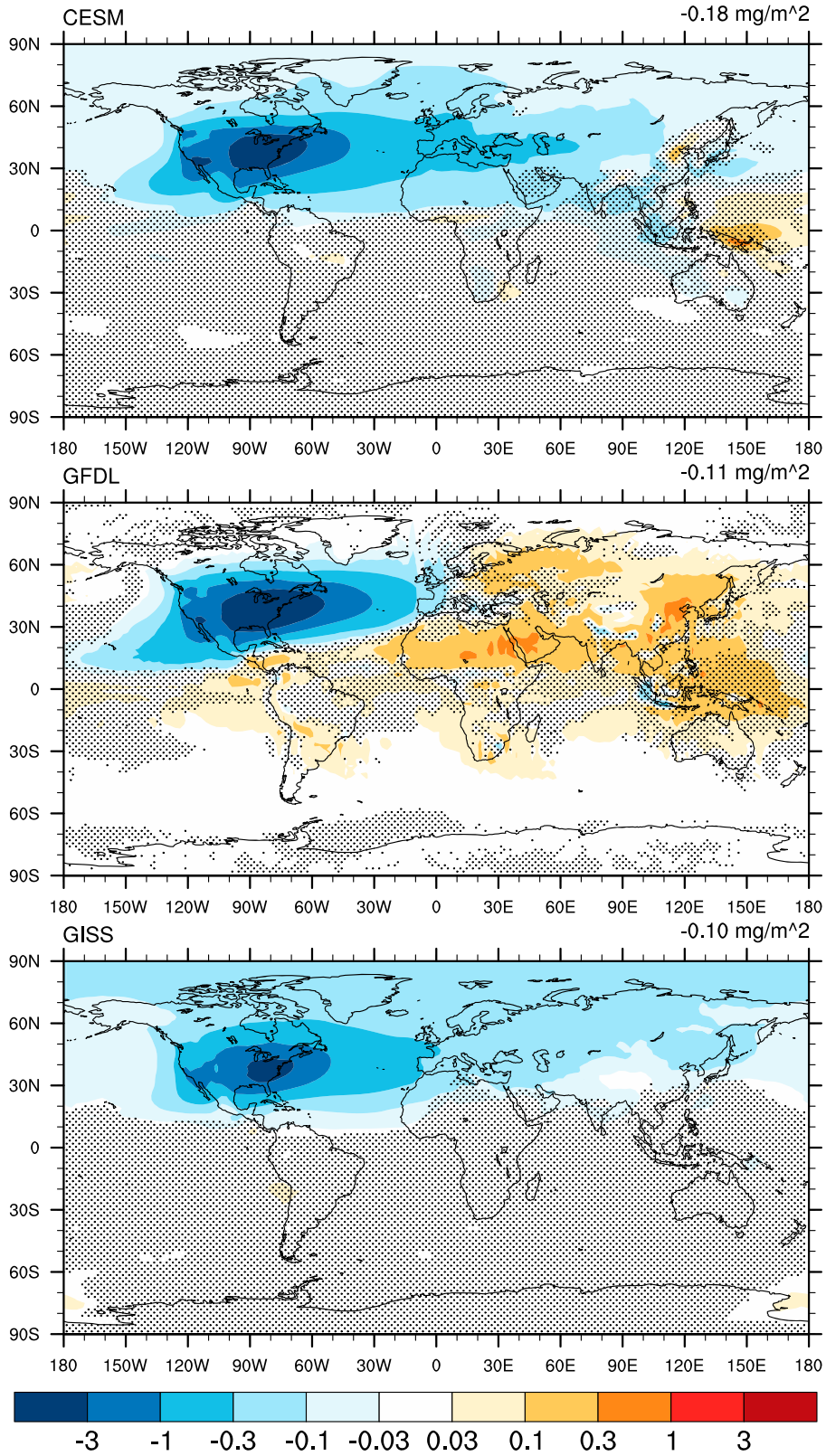

Figure 1. SO_4 burden change in mg m^{-2}. Note the logarithmic scale. The SO_4 burden changes most strongly over and downstream of the region of SO_2 emission changes. The global average value is in the upper right of each plot. Hatching indicates that no significant change is detected at the 2-sigma confidence level.

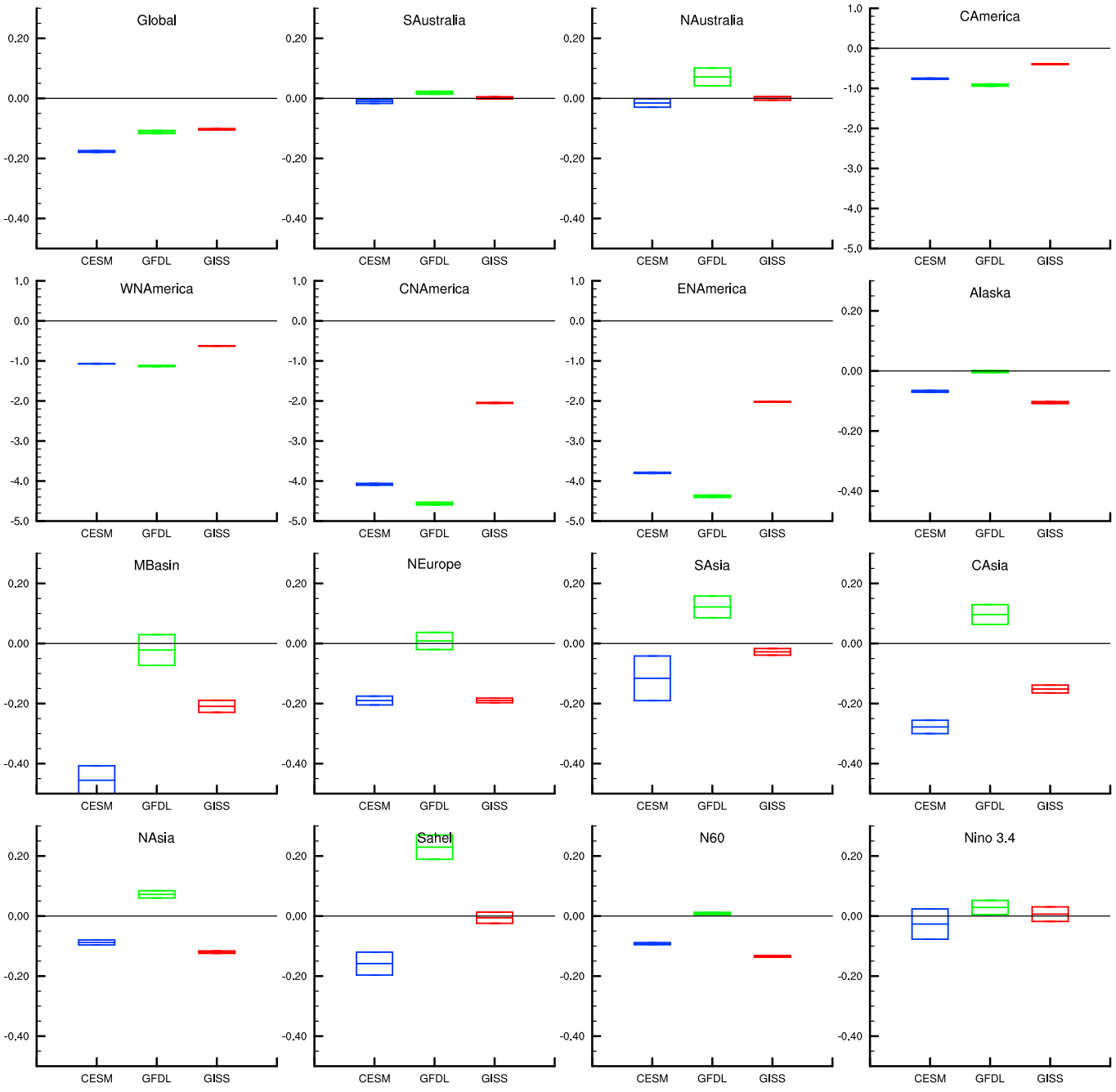

Figure 2. SO_4 burden change in mg m^{-2}. American regions are on a different scale. The center of each box is the mean change. The bar indicates confidence intervals of 1 standard error. Regions are defined in Table S1. Burden changes plotted for GISS exclude SO_4 on dust.

For the CESM model the burden change is 2.31 ± 0.16 mg m^{-2}. Assuming that the total burden of U.S. SO_4 is due to U.S. SO_2 emissions, these results are comparable. Precise comparison is difficult, since there are other sources of SO_4 such as DMS oxidation and transport from other regions.

Of the three models, the SO_4 burden decreases most in the GFDL model over all North American regions (Figure 2), consistent with the long lifetime in this model, which results in part from the weak removal of aerosols by convective precipitation (Fang et al., 2011; Paulot et al., 2016). In contrast to the other two models, the SO_4 burden in the GFDL model increases over the Sahel, Arabian Peninsula, and South East Asia (Figure 1).

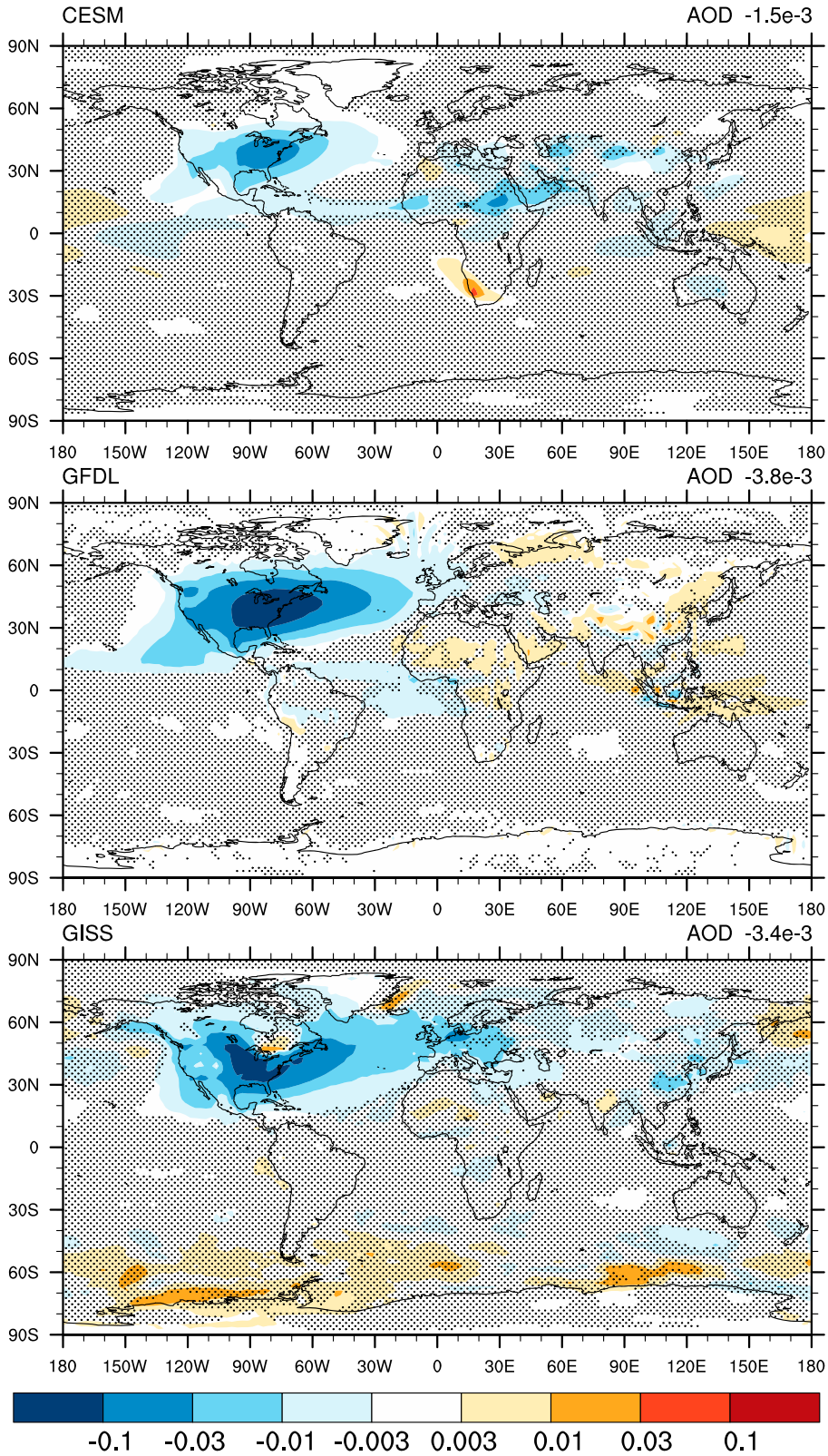

Figure 3. Aerosol optical depth change due to zeroing out U.S. SO_2 emissions. Global average value is in the upper right of each plot. Hatching indicates no detection of significant change at the 95% confidence level.

This opposite-signed response in remote regions versus the source region mutes the global average burden change in the GFDL model relative to the CESM model. In the section S8 we examine the effects of wet and dry removal on SO_4 lifetime in relation to this small remote increase in SO_4 burden. The lifetime over Northern Africa is 10 times longer than over the United States; however, the change in lifetime is large only near the source region. The precise cause of this small remote increase of SO_4 has not been diagnosed.

The largest global average SO_4 burden change occurs in CESM even though the burden change is slightly smaller than the GFDL model over the North American regions. The changes in the CESM and GISS SO_4 burden stretch further east, reaching across Europe, North Africa, and Central Asia. The SO_4 burden change in the GISS model is smallest (by a factor of 2–4) over the North American regions, consistent with the short SO_4 lifetime; the decrease north of 60°N is considerably stronger than the other models. There is almost no SO_4 burden change over Africa, South East Asia, or the Southern Hemisphere in the GISS model.

In summary, all three models show significant decreases in SO_4 over North America and downwind, to varying degrees, from that region of peak emission change. Model responses in remote regions differ, but those remote responses are small compared to the source-region responses, as can be expected from a short-lived climate forcer.

4. Aerosol Optical Depth Response and Impacts

SO_4 is a major contributor to AOD. Validation of the AOD against observations is difficult, due to the coarse resolution of these models, as can be seen in the supporting information of Westervelt et al. (2017), and in any case does not necessarily reveal the realism of the sulfate aerosol distribution. However, as mentioned above, these models have all been evaluated as part of CMIP5.

When U.S. anthropogenic SO_2 emissions are reduced, we find that global AOD decreases by 0.0015 to 0.0038 across the three models (Table 3). The optical depths are not precisely comparable, due to differences in physical parameterizations (e.g., internally mixed and externally mixed), diagnosis at slightly different wavelengths, or different assumptions for the indices of refraction for the materials in the aerosols; however, there may be some value in comparing patterns of change in optical depths. For all three models, the peak of the AOD response is over Eastern North America near the region of peak SO_4 burden response (Figure 3). All three models show a decreased AOD in the downwind region from the east coast of North America toward Europe, and those regions roughly correspond to the decreased SO_4 burden (Figure 1). Remote regions show relatively small changes in AOD (Figure 4).

The GFDL and GISS models show AOD changes as large as 0.1 in the Central and Eastern North America regions. The GFDL model shows small increases in AOD over regions where the SO_4 burden increased, such as the Sahel, North Asia, and South Asia.

In contrast to the other two models, the CESM model shows a strong local SO_4 burden change but the weakest AOD change (by a factor of 3 to 5) both in global average and in the North American regions. The MAM-3 aerosol model in CESM prognoses size distributions across three aerosol modes, all of which contain sulfate. This complex model leads to a more complex relationship between AOD and sulfate burden than in the GFDL and GISS models. Diagnosing how the sulfate contributes to optical properties of the aerosols is beyond the scope of this paper; however, these three models are distinct in their treatments of aerosol microphysics and it is not surprising that they have a diversity of AOD responses to SO_4 perturbations. In section S7 we construct effective cross sections by regressing change in optical depth against change in mass (Table S1). We see that the effective cross section of sulfate in the GFDL model is about 3 times the size of the CESM model, indicating a significant difference in optical properties. In addition, as seen in Figure S11, the residual optical depth indicates an inconsistency between sulfate mass and sulfate optical depth for the GFDL model, consistent with relative humidity across the U.S. leading to the expectation that the stronger optical depth response in the GFDL model could be due to a larger hygroscopic response in that model compared to the CESM model. A complete understanding of this difference would require additional diagnostic computations.

Beyond the AOD responses due to sulfate, there is also a significant global dust AOD response in all three models (Table 3). Both the GFDL and CESM models show decreased dust optical depth over the Sahel and

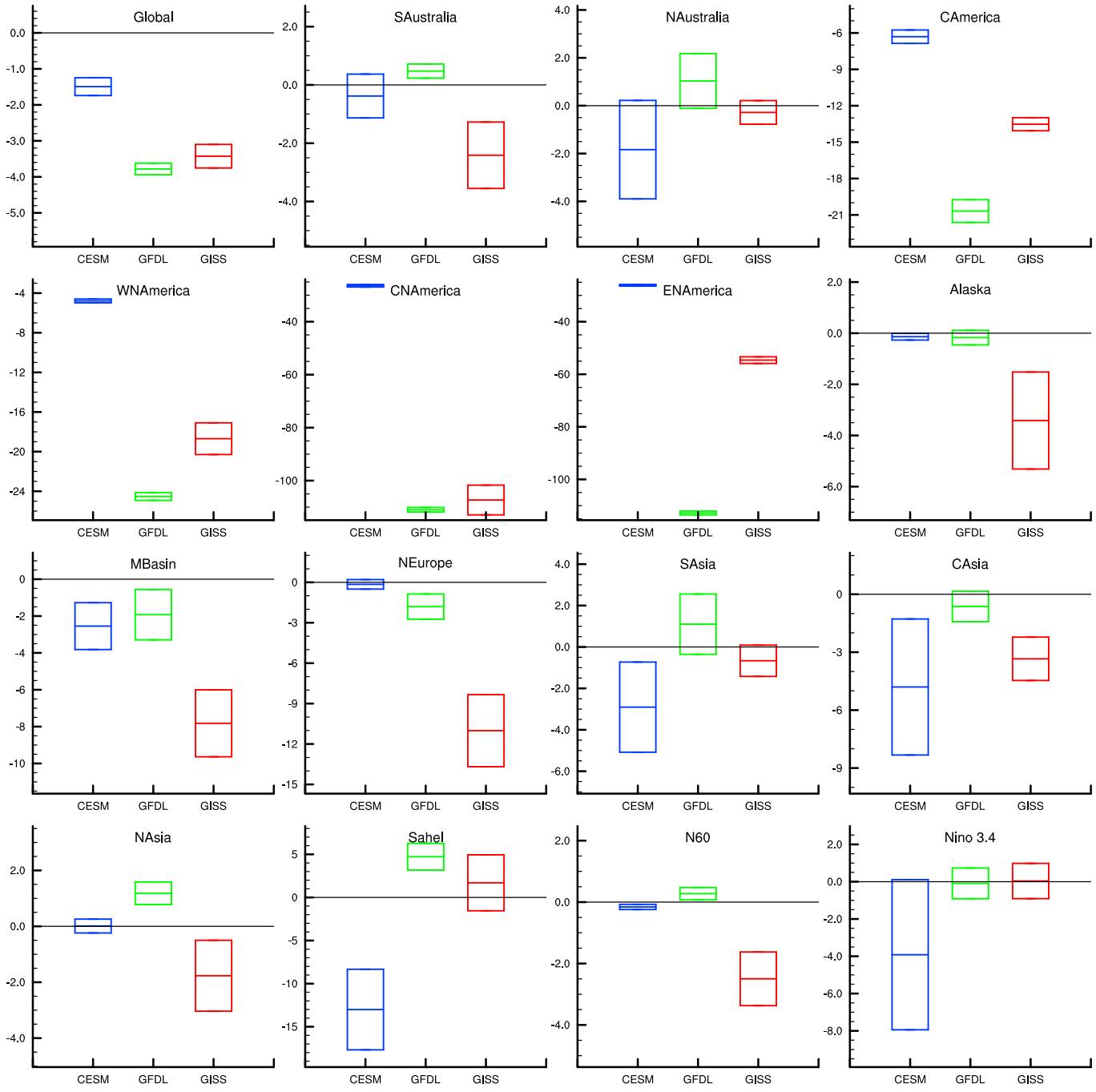

Figure 4. Aerosol optical depth response to zeroing out U.S. SO_2. Note the large scales in the North American regions. Units are 10^{-3} OD.

downwind to Central America (Figure 5). Additionally, the GFDL model shows (Figure 6) significant decreases over South Asia and Central Asia and increases over Eastern North America, Northern Europe, Northern Asia, and North of 60°N. Dust response in the GISS model is much smaller and significant at a few grid points; however, the reliability of these few significant points is questionable, given that about 5% of grid points would be found to be significant, given random draws from identical distributions. The CESM model only shows significant response in the Sahel and Central America regions; however, the patterns of dust response (Figure 5) are somewhat similar between the CESM and GFDL models. The increased dust optical depth in the CESM

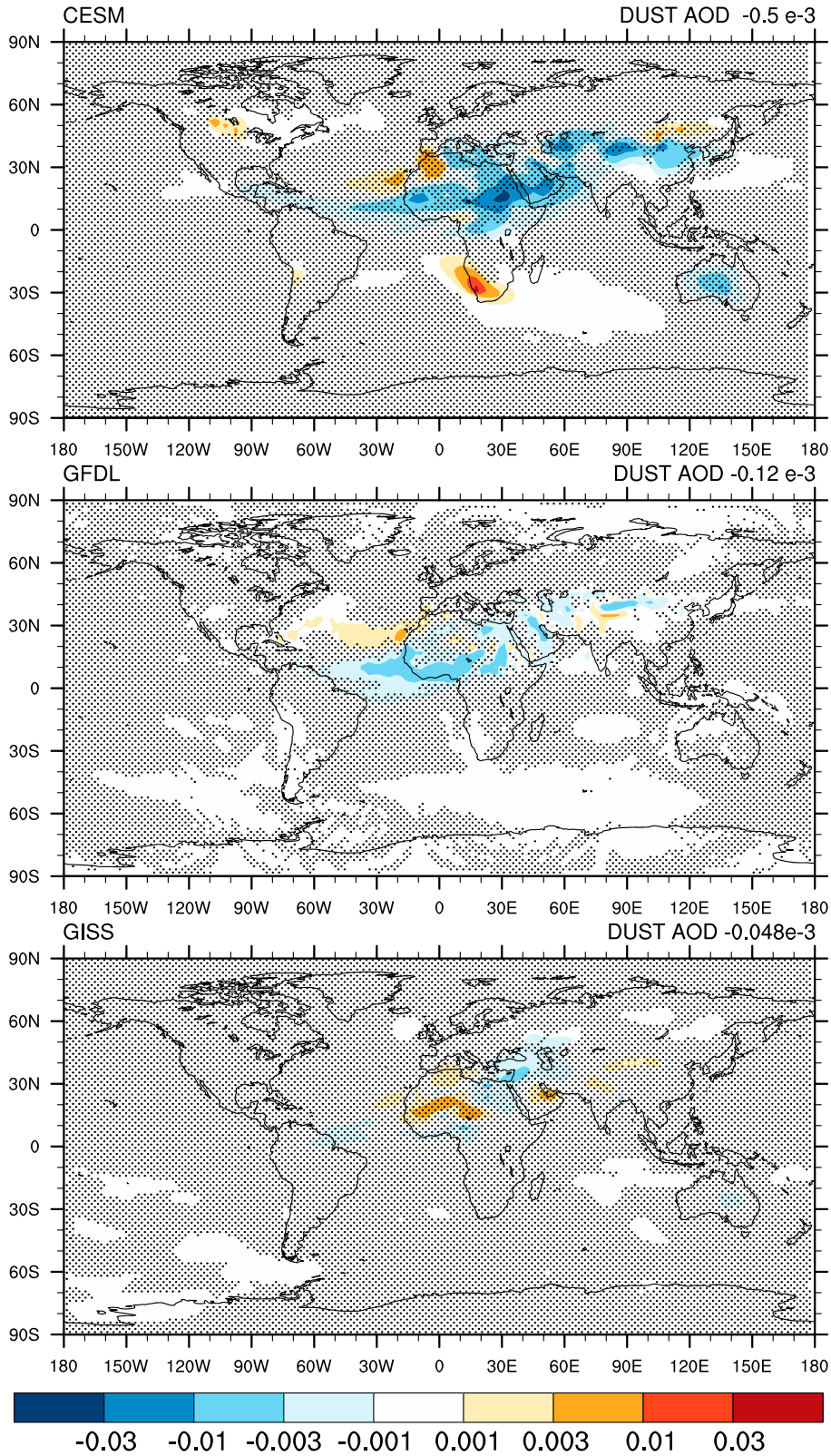

Figure 5. Change in dust optical depth due to zeroing out U.S. SO_2 emissions. Global average value is in the upper right of each plot. Hatching indicates that significant change is not detected at the 95% level.

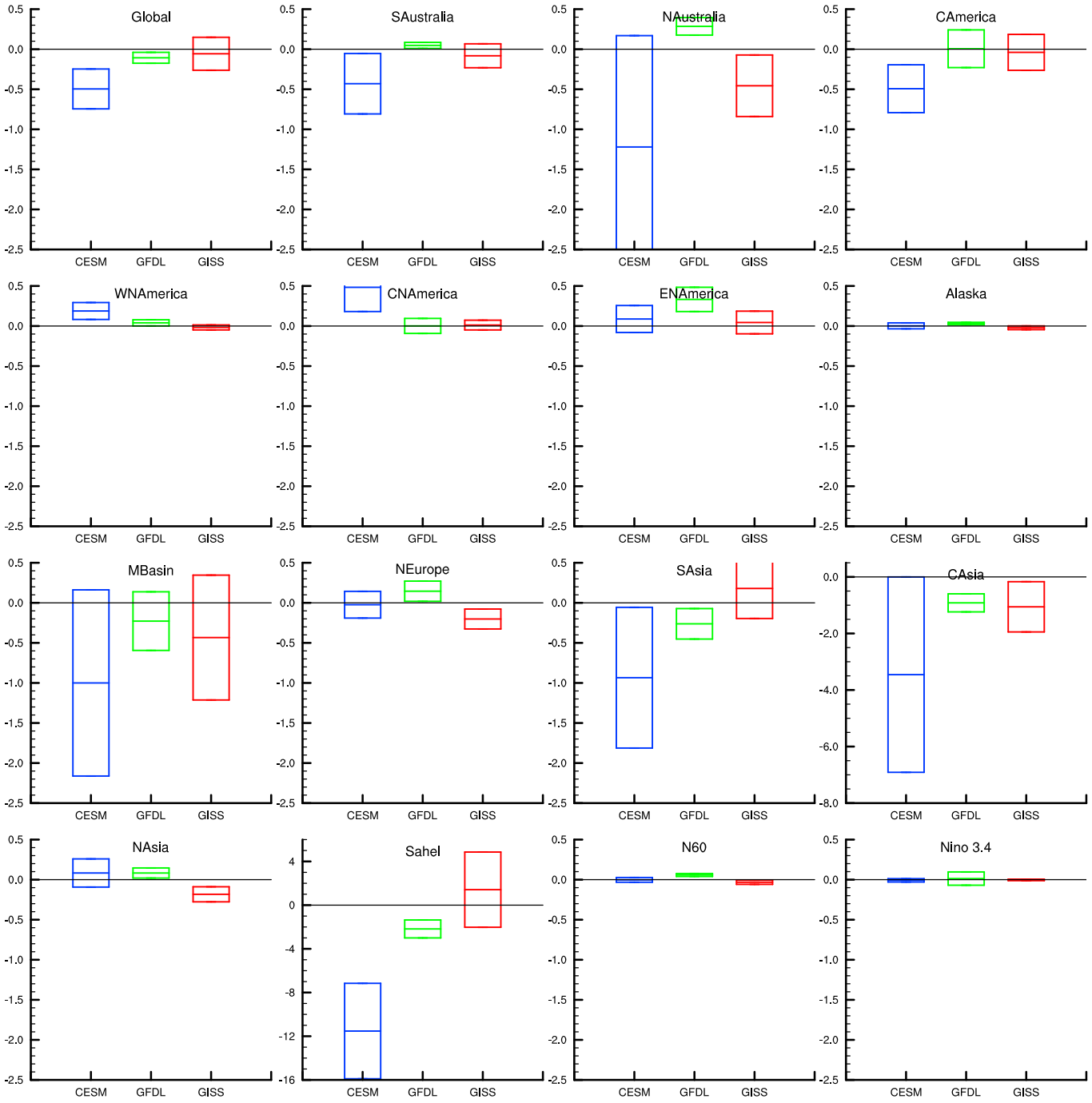

Figure 6. Change in dust optical depth in each region due to zeroing out US SO_2 emissions. Units are (10^{-3} OD). The Sahel and Central Asia regions are plotted on much larger scales. Note that scale is specific to each region.

model (compared to the GFDL model) is due to an increased mass response (cf. Figures S8 and S10) rather than differences in optics (Table S1).

For both the CESM and GFDL models, the dust optical depth west of Africa increases north of 20°N and decreases south of 20°N over the Atlantic from the west coast of Africa through the southern Caribbean. The decreased dust optical depth would be consistent with the increased Sahel precipitation seen in these simulations as documented in Westervelt et al. (2017); however, in the GFDL model, the dust emissions are

Table 4
Effective Radiative Forcing Simulation Results

Effective radiative forcing simulations	CESM	GFDL	GISS
ERF (W m^{-2})	0.16 ± 0.04	0.17 ± 0.04	0.053 ± 0.017
Δ AOD (10^{-3})	−2.3 ± 0.5	−5.3 ± 0.5	−3.4 ± 0.3
Δ AOD_Dust (10^{-3})	−0.9 ± 0.3	−0.49 ± 0.02	−0.15 ± 0.05
Forcing Sensitivities			
ERF/Δ Emissions [W m^{-2} (Tg SO_2 $year^{-1})^{-1}$]	−0.011 ± 0.003	−0.011 ± 0.003	−0.004 ± 0.001
ERF/Δ AOD (W m^{-2} AOD^{-1})	−68. ± 22.	−32. ± 8.	−16. ± 5.
Coupled-model temperature response to forcing			
Δ *T*/ERF (K (W $m^{-2})^{-1}$)	0.44 ± 0.18	0.68 ± 0.19	0.98 ± 0.42

Note. Also, the global-average temperature change from coupled simulations per global-average forcing from ERF computations.

independent of soil moisture and precipitation. We speculate that wet removal may be playing a part in the decreased dust optical depth.

In summary, AOD responses are strongest in the North American regions near to and downwind from the region of decreased SO_2 emissions. The two models with strong forcing over the eastern U.S. (see below) also show similar and significant patterns of dust response over (and west of) Africa. Quantitative comparisons of both AOD sensitivities to SO_4 as well as comparisons of AOD response in remote regions are limited due to the nonrobust signals across models (Figure 6).

5. Effective Radiative Forcing and Aerosol Feedback

The ERF due to decreased U.S. SO_2 emissions includes full adjustment of the atmosphere and land models, including dust aerosol responses from changes in emissions, transport, and deposition. As mentioned in section 2.7, the ERF calculations use the same climate models, but forced with specified SST and SIC distributions. Note that each modeling group uses their own specification, but they critically use the same distribution in the control and perturbation calculations. We have found (in CESM) very little sensitivity to the choice of specified SST/SIC distributions whether from observations or model simulations for the same period.

All three models include both aerosol-radiation and aerosol-cloud interactions, albeit to differing degrees of complexity. The models include distinct characterizations of aerosol optics (affecting AOD), aerosol microphysics (affecting size distributions and optics), and indirect effects (affecting clouds). In particular, in this GISS model version, aerosols do not affect the cloud lifetime.

The CESM and GFDL models have similar global ERF of about 0.16 W m^{-2}, while the GISS model is a factor of 3 smaller (Table 4). In comparison, the Atmospheric Chemistry and Climate Model Intercomparison Project (ACCMIP) studies show a similar ratio of 2.5 between the GFDL and GISS model for total global SO_4 forcing (Table 5) (Shindell, Lamarque, et al., 2013). Gettelman et al. (2015) similarly show a factor of about 2 between CESM and GISS for total aerosol radiative effect between 2000 and 1850 with indirect effects being nearly twice as strong in CESM as in GISS; which could be associated with the lack of a cloud lifetime effect in GISS.

Table 5
Effective Radiative Forcing Simulation Results From Other Studies

Effective radiative forcing simulations	CESM	GFDL	GISS
Global total SO_4 aerosol ERF (ACCMIP 2000–1850) (Shindell, Lamarque, et al., 2013)		−1.64	−0.61
Temperature response to forcing			
CO_2: Δ *T*/ERF (K [W $m^{-2}]^{-1}$)	1.1[a]	1.32[b]	0.56[b]

[a]CO_2 temperature response of 4.1 K due to a forcing of 3.7 W m^{-2} in CESM1 (Meehl et al., 2013). [b]GFDL temperature response of 3.97 K for a forcing of 2.99 W m^{-2} and GISS temperature response of 2.11 K for a forcing of 3.78 (Forster et al., 2013).

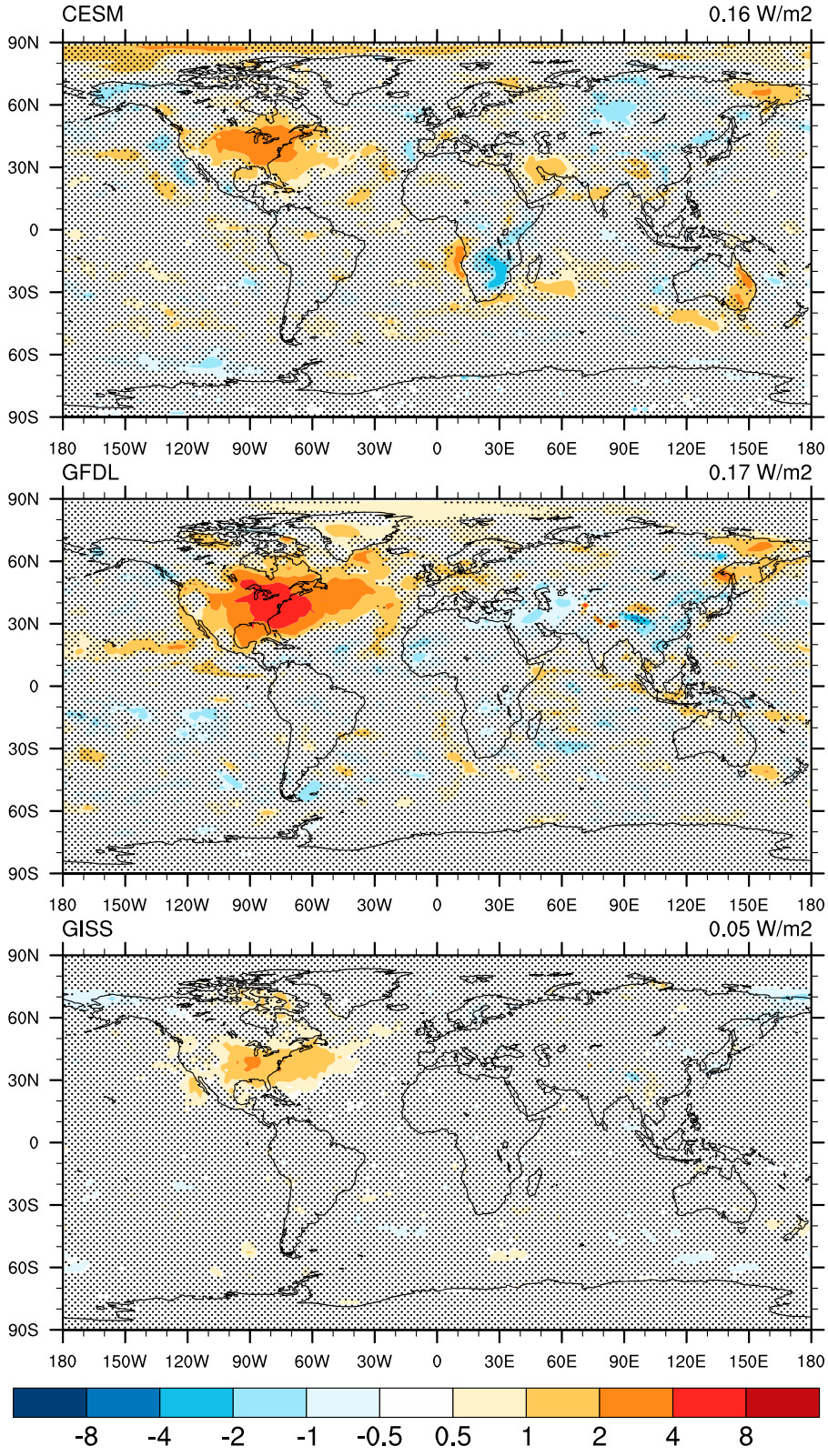

Figure 7. Effective radiative forcing in W m^{-2} due to zeroing out U.S. SO_2 emissions. Global average value is in the upper right of each plot. Hatching indicates that no significant change was detected.

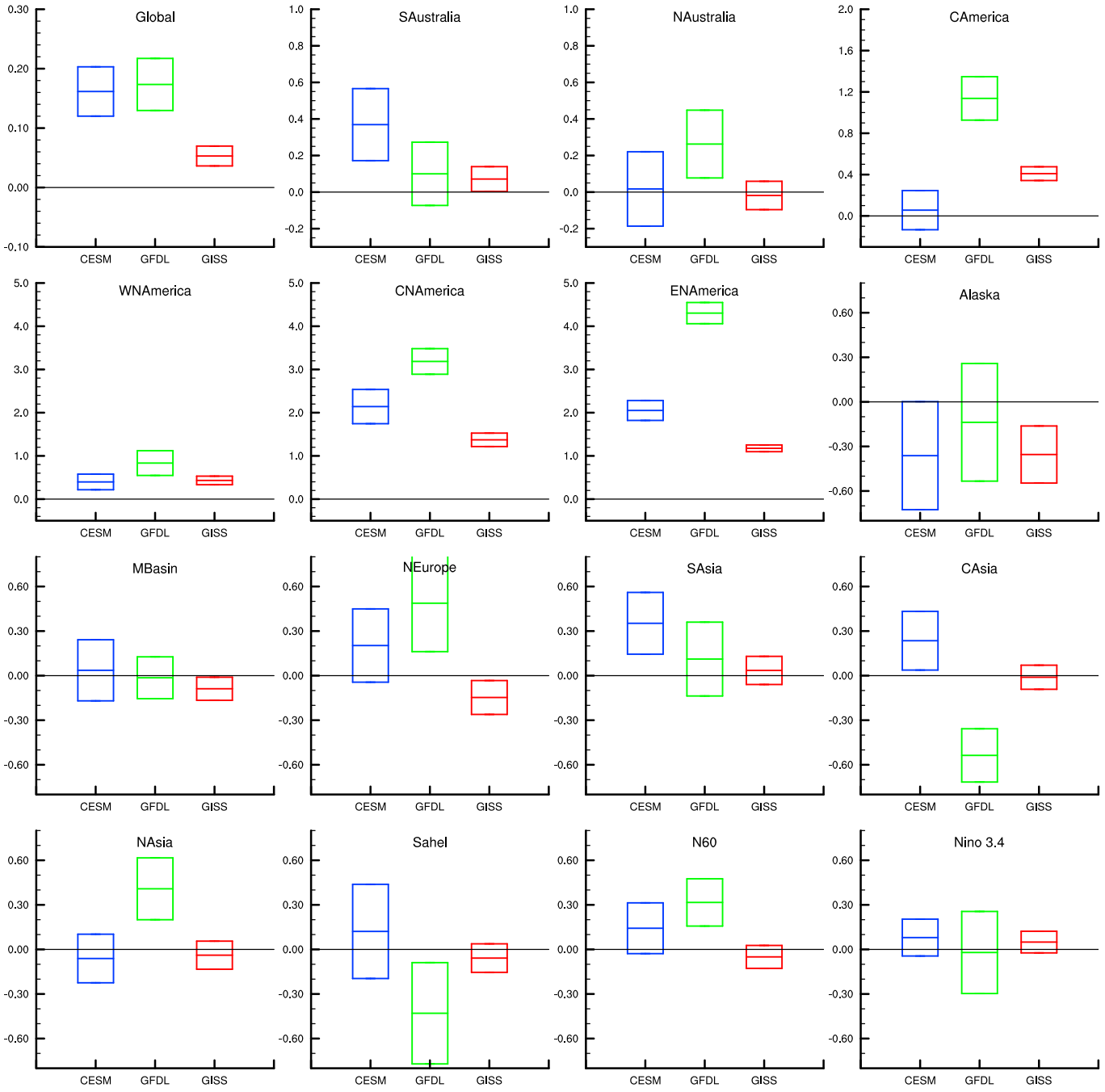

Figure 8. Effective radiative forcing in W m^{-2} due to zeroing out U.S. SO_2 emissions. Note the scale change for the Global, American, and Australian regions.

Qualitatively in all three models, the region of peak forcing corresponds closely with the region of peak AOD and SO_4 change. However, the forcing per unit change in AOD varies by a factor of 4 between these models. Similarly, the forcing per change in AOD in the ACCMIP studies (Shindell, Lamarque, et al., 2013) showed a median value of -30 W m^{-2} AOD^{-1} with a 95% confidence range of -660 to -15. In our case, CESM tends to display a relatively strong forcing per change in AOD, while the GISS model shows a relatively weak forcing per change in AOD.

In all three models, the global-average dust optical depth is about a factor of 3 stronger in these forcing computations compared to the climate simulations. There are numerous aerosol species that are adjusting along

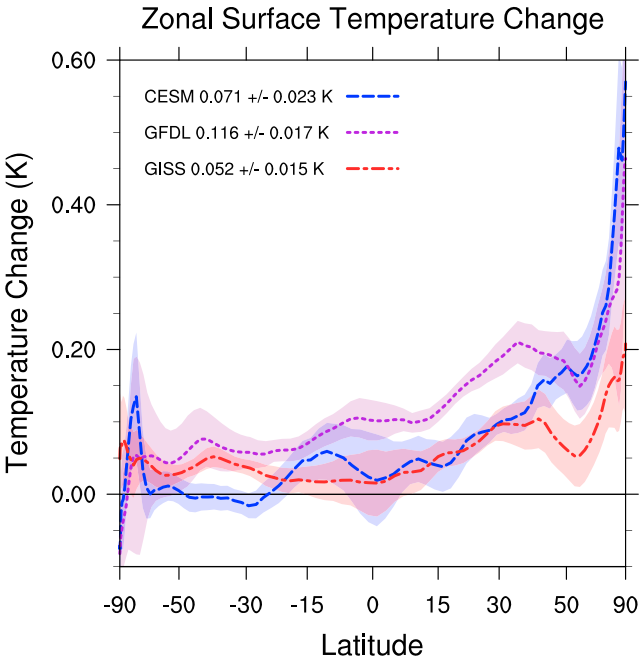

Figure 9. Zonal-average surface temperature response in K due to zeroing out U.S. SO_2 emissions. The shaded regions show the temporal standard error in the annual time series of zonal averages. The global average value is listed for each model in the legend.

with the rest of the atmosphere and land. It appears that the use of specified SST and SIC leads to distinct meteorological responses, that in turn creates dust responses, which are larger than those in the coupled ocean simulations, highlighting the challenge of accurately diagnosing ERF that includes rapid responses. In spite of this feedback (up to 30% of the total AOD response in the case of CESM), there is no clear indication of an associated local radiative perturbation due to this dust response (Figure 7), and hence, in this case the ERF values appear suitable for comparison with the climate response. Indeed, dust forcing efficiency can be muted due to the fact that the top of atmosphere radiative effect of shortwave scattering is of opposite sign to the shortwave and longwave absorption of dust.

As can be expected from the geographical distribution of ERF (Figure 7), the radiative forcing in remote regions is smaller by at least a factor of 5 relative to the North American regions in all three models (Figure 8). In these remote regions, the forcing is rarely statistically significant and tends to be inconsistent between models. Additional years of forcing computation would be required to compare remote forcing estimates as can be seen by the decreased noise in the remote regions of the GISS estimates seen in Figure 7. The GISS model simulated approximately 3 times as many years (160 compared to 50 years), leading to decreased noise and narrower confidence ranges (Figure 8) in remote regions. In contrast, latter sections of this paper will show significant and robust temperature changes in some remote regions in spite of the lack of top-of-atmosphere forcing in remote regions.

To summarize, quantitative changes in forcing per change in AOD are some of the least robust sensitivities between models; however, qualitatively, the peak change in AOD is in the regions where both SO_4 burden change and ERF peak. Many aspects contribute to this lack of connection between ERF and AOD; namely, indirect effects of aerosols, the fact that AOD is computed at a single frequency (band) of light, AOD does not distinguish between scattering and absorption and is independent of whether it is above clouds, beneath clouds, and AOD does not distinguish between bright and dark surfaces. In ERF computations, responses in other aerosols can also confound the connection between ERF and AOD. While AOD is may be an observable quantity, it is not a great indicator of forcing. The ERF per change in SO_2 emission is more consistent across the models but still varies by a factor of 3 with a global average value of -0.009 W m^{-2} per (Tg SO_2 year^{-1}). Forcing in remote regions is much smaller and often insignificant.

6. Surface Temperature Response

In all three models the global surface temperature increases in response to the SO_4 decrease (Table 3), but the magnitude of this varies by a factor of 2 across models with the GFDL model having the largest response and GISS the smallest. Within the available 200 years of simulations, the confidence interval of the global average surface temperature response in the CESM model overlaps both the GFDL and GISS models; the only significant difference in global temperature response is between the GFDL and GISS models.

Regionally, all three models show the largest temperature increase in the Arctic (Figure 9) as well as warming over most of the northern hemisphere (Figure 10), although the CESM model shows less response (or possibly cooling) in a narrow band south of the Sahel, through the Arabian Peninsula, North of the Himalaya, and across the Gobi Desert. However, these patterns in the CESM model are insignificant at the 2-sigma level. In addition, CESM generates a negative PDO-like pattern (Pacific Decadal Oscillation; Mantua & Hare, 2002) in response to U.S. SO_2 removal. This pattern is also not significant, but it contributes to a reduction in the diagnosed global-average surface warming. In the Southern Hemisphere the three models indicate that there may be warming, but the responses are small and rarely significant (Figures 10 and 11). The simulated range of temperature responses is not surprising given the range of SO_4 burden changes, AOD changes, differences in microphysical parameterizations, and climate sensitivities. As previously discussed, the ERF per unit change

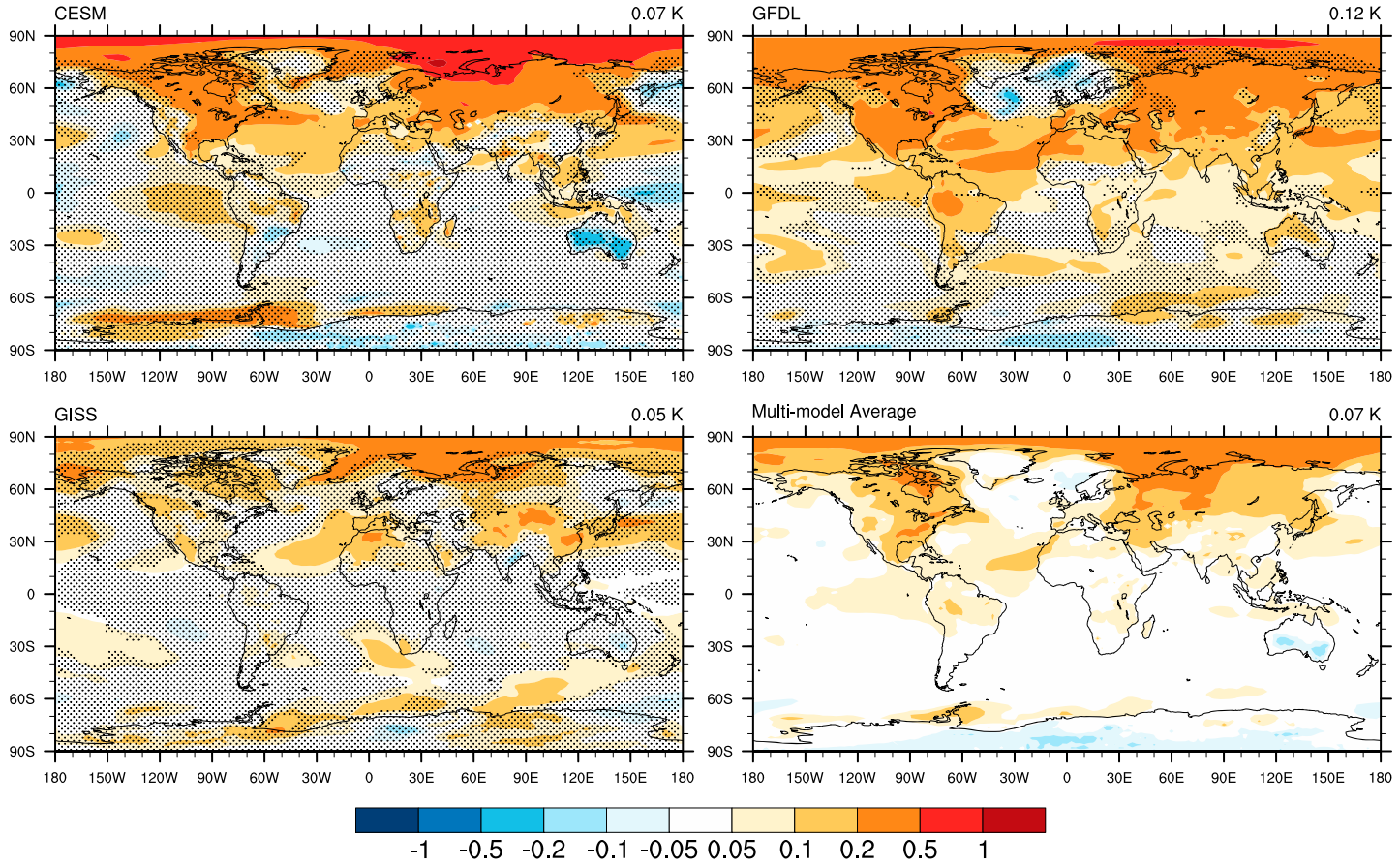

Figure 10. Surface temperature response in K due to zeroing out US SO_2 emissions. Hatching indicates that no significant change was detected at the 95% level. The multimodel average is an unweighted average of the three models. The multimodel average plot shows no shading for significance. The global average change is indicated in the upper right of each plot.

in emissions varies by a factor of 3 across models, and the ERF per change in AOD ranges by a factor of 4. In spite of the spread of intermediate responses, the temperature responses across models show a remarkable similarity of zonal pattern (Figure 9), especially given the small size of the forcing, suggesting that our experimental design and statistical methods were successful at providing a robust estimate of the forced response in the models.

While the temperature response shows similar patterns between models, global surface temperature sensitivity per unit forcing varies between these models not only in this study of SO_2 emissions but also in studies of CO_2 concentration changes. CESM, GFDL, and GISS have temperature sensitivities per forcing of 1.1, 1.32, and 0.56 K per (W m^{-2}), respectively, in doubled CO_2 experiments (Table 5). It should be noted that the computations of CO_2 forcing are based on Gregory et al. (2004) regression. In contrast, the global temperature sensitivities to SO_2 forcing (Table 4) are 0.44 ± 0.18, 0.68 ± 0.19, and 0.98 ± 0.42 K per (W m^{-2}), respectively. Not only are the sensitivities between models different, but the sensitivity to forcing seems to also depend on the type of forcer (CO_2 versus SO_2) or perhaps the magnitude of the forcing. However, it is difficult to compare sensitivities between models or even to obtain the same sensitivities in a single model; for example, the equilibrium climate sensitivity due to doubled CO_2 for the same GFDL model version has been estimated at 4.6 K (Winton et al., 2013) and 3.97 K (Forster et al., 2013). The fact that the temperature response to forcing appears to be so different between CO_2 and the SO_2 emissions studied here indicates the need to consider other effects such as dynamical responses, removal and emission processes for other aerosols, and land (with a rapid response) versus ocean responses when evaluating forcing. We also note that these average responses include responses from early years after branching (20 years); thus, a comparison with

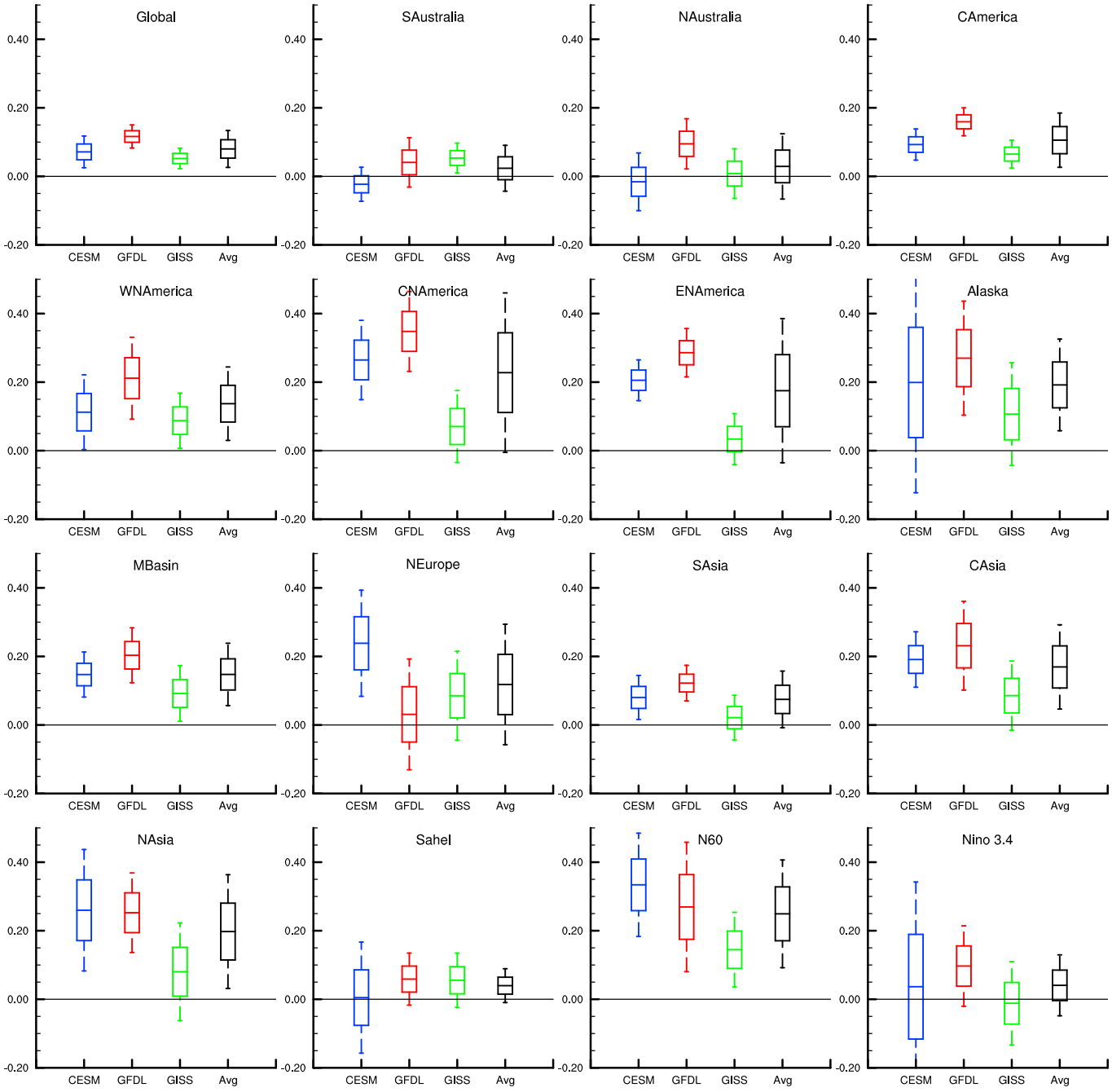

Figure 11. Surface temperature response in K due to zeroing out U.S. SO_2 emissions. For each model, the error bars indicate 68% confidence intervals and the whiskers indicate 95% confidence intervals of the mean response (i.e., 1 and 2 standard errors respectively). "Avg" indicates the average of the three model-mean responses, with 1 and 2 standard deviations of those responses indicated by the error bars and whiskers, respectively, using no weighting for skill or for confidence in each model.

equilibrium response is not consistent. Finally, the varying efficacy of various forcings has been previously studied by Hansen et al. (2005) and Shindell et al. (2015).

Ocean state has been shown to be important in estimates of ocean heat uptake due to CO_2 forcing, leading to inconsistent estimates of transient climate sensitivities (He et al., 2017) having a particularly strong connection to formation of dense sinking water in the North Atlantic. The forcing near the North Atlantic could be

possibly driving changes in deep water formation in the coupled system, affecting the ocean heat uptake differently between our models.

7. Discussion and Conclusion

We have used three Earth System models to analyze the simulated surface temperature change due to the removal of U.S. anthropogenic SO_2 emissions in constant-forcing multicentury perturbation experiments. These three models cover a range of parameterizations such as aerosol microphysics, cloud microphysics, dynamics, transport, and radiative transfer. Detecting the surface temperature responses with 68% confidence requires roughly 200 years for most of these models. Since *z*-score (and *t*-score for large sample size) is directly related to the square root of the number of independent samples, 800 years would be required to shrink the confidence intervals by a factor of 2.

While many aspects of the models are diverse, the model simulations show robust patterns of temperature responses over land. The temperature responses are strongest toward the Arctic but are positive for most of the northern hemisphere land regions. The more zonal pattern of temperature response as well as the greater response over land areas is consistent with prior analyses (Myhre et al., 2013; Rotstayn et al., 2014; Shindell, 2012; Shindell et al., 2015) (and rather distinct from the much more localized response found in the single-model study of Leibensperger et al., 2012).

All three models show a significant dust optical depth feedback. The simulations to diagnose ERF show a stronger dust optical depth decrease compared to the climate simulations. This feedback should be examined in subsequent studies in which there are sufficient diagnostics to identify the mechanisms underlying the dust responses.

The models differ in some other facets of the overall responses to decreasing U.S. SO_2 emissions. In the North American regions, CESM shows an AOD change per SO_4 burden change that is about one fourth the size of the other models and it shows a particularly large SO_4 burden change. The GISS model shows a smaller SO_4 burden change compared to the other models near the source region; this small burden change is consistent with its shorter SO_4 lifetime. The GFDL model shows an increase in SO_4 burden over the northern hemisphere portions of Africa and Asia; as a consequence, the global SO_4 burden change is not as strong as the burden changes in North America would imply.

AOD changes are difficult to interpret as they show some of the least robust responses and least robust sensitivities. Kasoar et al. (2016) also see a factor of 6 difference in AOD responses between the models they examined which included versions of the GISS and CESM models used here; furthermore, in that study the CESM AOD response was stronger than GISS in the source change region (China). We find here a stronger AOD response in GISS than in the CESM models in the source change region (United States). It is unclear why these studies would reverse rankings of AOD sensitivities although the response of AOD to emissions could be sensitive to factors such as background oxidation capacity and the abundance of other aerosols.

While the peak AOD change is near the region of SO_2 emission changes in all three models, the magnitude of AOD change varies greatly between models. SO_4 response per SO_2 emission reduction varies by 50%, AOD response per SO_4 response is not robust, forcing per AOD response is not robust, and temperature response per forcing is not robust. For instance, the global annual forcing per change in AOD varies by a factor of 4 between models. Temperature sensitivity per AOD change varies by a factor of 3 with CESM at the strongest and GISS at the weakest. AOD is a diagnostic quantity that could be compared with observations; however, given the range of parameterizations of aerosol and cloud microphysical specifications and processes, there is little reason to expect this observable diagnostic to imply a strong connection to forcing, to changes to cloud properties, or to SO_4 burden changes.

The radiative forcing in these models peaks near (and a little downwind from) the region of peak AOD changes. The radiative forcing is robustly stronger over North America than in remote regions. Global forcing per change in emission varies by a factor of 3 between models. The average global forcing per SO_2 emission change is -0.009 W m^{-2} per (Tg SO_2 year^{-1}) for the removal of anthropogenic U.S. SO_2 emissions.

Comparing fully coupled simulations with fixed sea surface (forcing) simulations, we see a dust optical depth response, which is 2 to 4 times as large in the forcing simulations as in the climate simulations in all three

models. This feedback is a significant part of the total AOD feedback in the CESM and GFDL models. The dust feedback is a robust response, even if the magnitude varies between models. Shindell (2014) finds that transient climate sensitivity triggers more rapid land response and stronger feedback. The temperature response over Africa in the forcing simulations (where SSTs are held fixed to diagnose ERF) differs from the climate simulations (with full coupling between the atmosphere, ocean, and sea ice), indicating some distinct meteorological responses; however, a complete evaluation of the mechanism of this feedback will require additional simulations and diagnostics.

The temperature response is much more consistent between models. The magnitude of global average surface temperature response is within a factor of 2 between models. All three models show warming over most of the northern hemisphere land surface, with an amplified response in the Arctic (cf., Shindell, 2007). Southern Hemisphere temperature responses are not robust, large, or significant in this study, with the exception of the GFDL model, which shows some significant warming in some regions. While one might expect the largest temperature changes in central North America (near the region of peak forcing), the temperature responses in remote regions, such as Asia, are comparable.

The sensitivity of temperature to forcing is strongest in the GISS model and weakest in the CESM model; however, the ranges statistically overlap. This sensitivity is distinctly different from the CO_2 forcing sensitivity in which GISS is the weakest and GFDL and CESM are about a factor of 2 larger. The way in which the climate responds to a short-lived climate forcing seems to be different from a well-mixed climate forcer such as CO_2; however, CO_2 forcing is much larger and could trigger stronger feedback and the CO_2 forcings were computed with different methods from the sulfate ERFs used here.

Global temperature sensitivities per SO_4 burden change are different by a factor of 3 with GFDL at the strongest extreme and GISS at the weakest extreme. The models in average yield a temperature sensitivity per SO_2 emission change of -0.0055 ± 0.0021 K per (Tg SO_2 year^{-1}). The pattern of surface temperature responses is relatively similar between models over the northern hemisphere land surfaces. For comparison, Kasoar et al. (2016) find sensitivities to China emissions of 0.0068, -0.0016, and 0.0067 K per (Tg SO_2 year^{-1}) in the HadGEM3-GA4, GISS-E2, and CESM models, respectively (with large standard error estimates on the GISS-E2 results).

The surface temperature responses over Western, Central, and Eastern North America land surfaces are roughly 0.12, 0.24, and 0.19 K, respectively. For comparison, the transient combined anthropogenic and natural North American transient temperature change seen since 1970 in the CMIP5 ensemble average is roughly 1 K (Boucher et al., 2013; Jones et al., 2013). While a comparison of equilibrium and transient responses is not rigorous, the fact that the global-average surface temperature responses to U.S. SO_2 emissions are approximately 10–25%, the size of the transient response to combined anthropogenic emissions indicates the significance of the U.S. SO_2 emissions. Similarly, we see an average temperature response in our simulations of about 0.2 K over Northern Asia and in observations of more than 1.7 K (cf., Figure 1 in IPCC (2013)). The contribution from U.S. SO_2 emissions seems to be a smaller portion of the surface temperature change seen in the Northern Asia region when compared to the response in the North American regions.

There is a robust surface temperature response to removal of U.S. SO_2 emissions in remote northern hemisphere regions. Land surfaces at similar latitudes experience similar responses. The amplification of warming over the Arctic, in spite of a relatively small forcing there, also indicates a strong remote temperature response to short-lived climate forcers from non-Arctic regions (e.g., Shindell, 2007), as has also been well established to occur for well-mixed greenhouse gases (Bony et al., 2006; Holland & Bitz, 2003; Masson-Delmotte et al., 2006; Moritz et al., 2002).

In a following paper, we will be expanding this analysis to a broader range of forcing agents and forcing regions, with the ultimate goal of generating source-response functions, within the limits of the identified statistical significance.

Acknowledgments

Data as well as plotting routines are available from Zenodo https://zenodo.org/record/1182767 (Conley, 2018). We would like to acknowledge the significant, helpful, and constructive reviews that improved earlier versions of this paper. Funding for this study was provided by an NSF EaSM-3 grant AGS 14-19398. The authors declare no conflicts of interest, and views, opinions, and findings presented in this paper are solely those of the authors and do not reflect the views of the funding agency. The NCAR-CESM work is supported by the National Science Foundation and the Office of Science (BER) of the U.S. Department of Energy. NCAR is sponsored by the National Science Foundation. We thank the NASA High-End Computing Program through the NASA Center for Climate Simulation at Goddard Space Flight Center for computational resources.

References

Abdul-Razzak, H., & Ghan, S. J. (2000). A parameterization of aerosol activation 2. multiple aerosol types. *Journal of Geophysical Research*, *105*(D5), 6837–6844.

Akaike, H. (1974). A new look at the statistical model identification. *IEEE Transactions on Automatic Control*, *19*(6), 716–723. https://doi.org/10.1109/TAC.1974.1100705

Anderson, J. L., Cai, W., & Walsh, K. (2004). The new GFDL global atmosphere and land model AM2–LM2: Evaluation with prescribed SST simulations. *Journal of Climate*, *17*(24), 4641–4673. https://doi.org/10.1175/JCLI-3223.1

Andrew J. Conley (2018). Surface-Temp-Impacts-from-US-SO_2: Initial release of data (Version v1.0). Zenodo. https://doi.org/10.5281/zenodo.1182767

Bollasina, M. A., Ming, Y., & Ramaswamy, V. (2011). Anthropogenic aerosols and the weakening of the South Asian summer monsoon. *Science*, *334*(6055), 502–505. https://doi.org/10.1126/science.1204994

Bony, S., Colman, R., Kattsov, V. M., Allan, R. P., Bretherton, C. S., Dufresne, J. L., et al. (2006). How well do we understand and evaluate climate change feedback processes? *Journal of Climate*, *19*(15), 3445–3482. https://doi.org/10.1175/JCLI3819.1

Booth, B. B., Dunstone, N. J., Halloran, P. R., Andrews, T., & Bellouin, N. (2012). Aerosols implicated as a prime driver of twentieth-century North Atlantic climate variability. *Nature*, *484*(7393), 228–232. https://doi.org/10.1038/nature10946

Boucher, O., Randall, D., Artaxo, P., Bretherton, C., Feingold, G., Forster, P., et al. (2013). Clouds and aerosols. In T. F. Stocker, et al. (Eds.), *Climate Change 2013: The Physical Science Basis, Contribution of Working Group I to the Fifth Assessment Report of the Intergovernmental Panel on Climate Change* (pp. 571–657). Cambridge, UK and New York, NY, USA: Cambridge University Press.

Bretherton, C. S., McCaa, J. R., & Grenier, H. (2004). A new parameterization for shallow cumulus convection and its application to marine subtropical cloud-topped boundary layers. Part I: Description and 1D results. *Monthly Weather Review*, *132*(4), 864–882. https://doi.org/10.1175/1520-0493(2004)132%3C0864:ANPFSC%3E2.0.CO;2

Bretherton, C. S., Smith, C., & Wallace, J. M. (1992). An intercomparison of methods for finding coupled patterns in climate data. *Journal of Climate*, *5*(6), 541–560. https://doi.org/10.1175/1520-0442(1992)005%3C0541:AIOMFF%3E2.0.CO;2

Christidis, N., Stott, P. A., Zwiers, F. W., Shiogama, H., & Nozawa, T. (2012). The contribution of anthropogenic forcings to regional changes in temperature during the last decade. *Climate Dynamics*, *39*(6), 1259–1274. https://doi.org/10.1007/s00382-011-1184-0

Crawford, J. R., & Howell, D. C. (1998). Comparing an individual's test score against norms derived from small samples. *The Clinical Neuropsychologist*, *12*(4), 482–486. https://doi.org/10.1076/clin.12.4.482.7241

Dentener, F., Kinne, S., Bond, T., Boucher, O., Cofala, J., Generoso, S., et al. (2006). Emissions of primary aerosol and precursor gases in the years 2000 and 1750 prescribed data-sets for AeroCom. *Atmospheric Chemistry and Physics*, *6*(12), 4321–4344. https://doi.org/10.5194/acp-6-4321-2006

Donner, L. J., Wyman, B. L., Hemler, R. S., Horowitz, L. W., Ming, Y., Zhao, M., et al. (2011). The dynamical core, physical parameterizations, and basic simulation characteristics of the atmospheric component AM3 of the GFDL global coupled model CM3. *Journal of Climate*, *24*(13), 3484–3519. https://doi.org/10.1175/2011JCLI3955.1

Eyring, V., Bony, S., Meehl, G. A., Senior, C. A., Stevens, B., Stouffer, R. J., & Taylor, K. E. (2016). Overview of the Coupled Model Intercomparison Project Phase 6 (CMIP6) experimental design and organization. *Geoscientific Model Development*, *9*(5), 1937–1958. https://doi.org/10.5194/gmd-9-1937-2016

Fang, Y., Fiore, A. M., Horowitz, L. W., Gnanadesikan, A., Held, I., Chen, G., et al. (2011). The impacts of changing transport and precipitation on pollutant distributions in a future climate. *Journal of Geophysical Research*, *116*, D18303. https://doi.org/10.1029/2011JD015642

Flato, G., Marotzke, J., Abiodun, B., Braconnot, P., Chou, S. C., Collins, W., et al. (2013). Evaluation of Climate Models. Chapter 9. In T. F. Stocker, et al. (Eds), *Climate Change 2013: The Physical Science Basis. Contribution of Working Group I to the Fifth Assessment Report of the Intergovernmental Panel on Climate Change*. Cambridge, United Kingdom and New York: Cambridge University Press.

Forster, P. M., Andrews, T., Good, P., Gregory, J. M., Jackson, L. S., & Zelinka, M. (2013). Evaluating adjusted forcing and model spread for historical and future scenarios in the CMIP5 generation of climate models. *Journal of Geophysical Research: Atmospheres*, *118*, 1139–1150. https://doi.org/10.1002/jgrd.50174

Freidenreich, S. M., & Ramaswamy, V. (1999). A new multiple-band solar radiative parameterization for general circulation models. *Journal of Geophysical Research*, *104*, 31,389–31,409. https://doi.org/10.1029/1999JD900456

Gettelman, A., Shindell, D. T., & Lamarque, J. F. (2015). Impact of aerosol radiative effects on 2000–2010 surface temperatures. *Climate Dynamics*, *45*(7–8), 2165–2179. https://doi.org/10.1007/s00382-014-2464-2

Ghan, S. J., Liu, X., Easter, R. C., Zaveri, R., Rasch, P. J., Yoon, J. H., & Eaton, B. (2012). Toward a minimal representation of aerosols in climate models: Comparative decomposition of aerosol direct, semidirect, and indirect radiative forcing. *Journal of Climate*, *25*(19), 6461–6476. https://doi.org/10.1175/JCLI-D-11-00650.1

Gregory, J. M., Ingram, W. J., Palmer, M. A., Jones, G. S., Stott, P. A., Thorpe, R. B., et al. (2004). A new method for diagnosing radiative forcing and climate sensitivity. *Geophysical Research Letters*, *31*, L03205. https://doi.org/10.1029/2003GL018747

Hansen, J. E., Sato, M. K. I., Ruedy, R., Nazarenko, L., Lacis, A., Schmidt, G. A., et al. (2005). Efficacy of climate forcings. *Journal of Geophysical Research*, *110*, D18104. https://doi.org/10.1029/2005JD005776

He, J., Winton, M., Vecchi, G., Jia, L., & Rugenstein, M. (2017). Transient climate sensitivity depends on base climate ocean circulation. *Journal of Climate*. https://doi.org/10.1175/JCLI-D-16-0581.1

Hoesly, R. M., Smith, S. J., Feng, L., Klimont, Z., Janssens-Maenhout, G., Pitkanen, T., et al. (2017). Historical (1750-2014) anthropogenic emissions of reactive gases and aerosols from the Community Emission Data System (CEDS). *Geoscientific Model Development Discussion*, 1–41. https://doi.org/10.5194/gmd-2017-43

Holland, M. M., & Bitz, C. M. (2003). Polar amplification of climate change in coupled models. *Climate Dynamics*, *21*(3–4), 221–232. https://doi.org/10.1007/s00382-003-0332-6

Horowitz, L. W. (2006). Past, present, and future concentrations of tropospheric ozone and aerosols: Methodology, ozone evaluation, and sensitivity to aerosol wet removal. *Journal of Geophysical Research*, *111*, D22211. https://doi.org/10.1029/2005JD006937

Horowitz, L. W., Walters, S., Mauzerall, D. L., Emmons, L. K., Rasch, P. J., Granier, C., et al. (2003). A global simulation of tropospheric ozone and related tracers: Description and evaluation of MOZART, version 2. *Journal of Geophysical Research*, *108*(D24), 4784. https://doi.org/10.1029/2002JD002853

IPCC (2013). Summary for policymakers. In: climate change 2013: The physical science basis. In T. F. Stocker, et al. (Eds.), *Contribution of Working Group I to the Fifth Assessment Report of the Intergovernmental Panel on Climate Change* (Section B1, 6 pp.). Cambridge, United Kingdom and New York: Cambridge University Press.

Jones, G. S., Stott, P. A., & Christidis, N. (2013). Attribution of observed historical near surface temperature variations to anthropogenic and natural causes using CMIP5 simulations. *Journal of Geophysical Research: Atmospheres*, *118*, 4001–4024. https://doi.org/10.1002/jgrd.50239

Jones, R. H. (1975). Estimating the variance of time averages. *Journal of Applied Meteorology*, *14*(2), 159–163. https://doi.org/10.1175/1520-0450(1975)014%3C0159:ETVOTA%3E2.0.CO;2

Kasoar, M., Voulgarakis, A., Lamarque, J. F., Shindell, D. T., Bellouin, N., Collins, W. J., et al. (2016). Regional and global temperature response to anthropogenic SO 2 emissions from China in three climate models. *Atmospheric Chemistry and Physics*, *16*(15), 9785–9804. https://doi.org/10.5194/acp-16-9785-2016

Knutti, R., Sedláček, J., Sanderson, B. M., Lorenz, R., Fischer, E. M., & Eyring, V. (2017). A climate model projection weighting scheme accounting for performance and interdependence. *Geophysical Research Letters*, *44*, 1909–1918. https://doi.org/10.1002/2016GL072012

Lamarque, J. F., Bond, T. C., Eyring, V., Granier, C., Heil, A., Klimont, Z., et al. (2010). Historical (1850–2000) gridded anthropogenic and biomass burning emissions of reactive gases and aerosols: Methodology and application. *Atmospheric Chemistry and Physics*, *10*(15), 7017–7039. https://doi.org/10.5194/acp-10-7017-2010

Leibensperger, E. M., Mickley, L. J., Jacob, D. J., Chen, W. T., Seinfeld, J. H., Nenes, A., et al. (2012). Climatic effects of 1950–2050 changes in US anthropogenic aerosols—Part 1: Aerosol trends and radiative forcing. *Atmospheric Chemistry and Physics*, *12*(7), 3333–3348. https://doi.org/10.5194/acp-12-3333-2012

Li, J., Mao, J., Min, K. E., Washenfelder, R. A., Brown, S. S., Kaiser, J., et al. (2016). Observational constraints on glyoxal production from isoprene oxidation and its contribution to organic aerosol over the Southeast United States. *Journal of Geophysical Research: Atmospheres*, *121*, 9849–9861. https://doi.org/10.1002/2016JD025331

Liu, X., Easter, R. C., Ghan, S. J., Zaveri, R., Rasch, P., Shi, X., et al. (2012). Toward a minimal representation of aerosols in climate models: Description and evaluation in the Community Atmosphere Model CAM5. *Geoscientific Model Development*, *5*(3), 709–739. https://doi.org/10.5194/gmd-5-709-2012

Malavelle, F. F., Haywood, J. M., Jones, A., Gettelman, A., Clarisse, L., Bauduin, S., et al. (2017). Strong constraints on aerosol–cloud interactions from volcanic eruptions. *Nature*, *546*(7659), 485–491. https://doi.org/10.1038/nature22974

Mantua, N. J., & Hare, S. R. (2002). The Pacific decadal oscillation. *Journal of Oceanography*, *58*(1), 35–44. https://doi.org/10.1023/A:1015820616384

Masson-Delmotte, V., Kageyama, M., Braconnot, P., Charbit, S., Krinner, G., Ritz, C., et al. (2006). Past and future polar amplification of climate change: Climate model intercomparisons and ice-core constraints. *Climate Dynamics*, *26*(5), 513–529. https://doi.org/10.1007/s00382-005-0081-9

Masui, T., Matsumoto, K., Hijioka, Y., Kinoshita, T., Nozawa, T., Ishiwatari, S., et al. (2011). An emission pathway for stabilization at 6 W m^{-2} radiative forcing. *Climatic Change*, *109*(1–2), 59–76. https://doi.org/10.1007/s10584-011-0150-5

Meehl, G. A., Washington, W. M., Arblaster, J. M., Hu, A., Teng, H., Kay, J. E., et al. (2013). Climate change projections in CESM1 (CAM5) compared to CCSM4. *Journal of Climate*, *26*(17), 6287–6308. https://doi.org/10.1175/JCLI-D-12-00572.1

Meinshausen, M., Smith, S. J., Calvin, K., Daniel, J. S., Kainuma, M. L. T., Lamarque, J. F., et al. (2011). The RCP greenhouse gas concentrations and their extensions from 1765 to 2300. *Climatic Change*, *109*(1–2), 213–241. https://doi.org/10.1007/s10584-011-0156-z

Menon, S., Koch, D., Beig, G., Sahu, S., Fasullo, J., & Orlikowski, D. (2010). Black carbon aerosols and the third polar ice cap. *Atmospheric Chemistry and Physics*, *10*(10), 4559–4571. https://doi.org/10.5194/acp-10-4559-2010

Miller, R. L., Schmidt, G. A., Nazarenko, L. S., Tausnev, N., Bauer, S. E., DelGenio, A. D., et al. (2014). CMIP5 historical simulations (1850–2012) with GISS ModelE2. *Journal of Advances in Modeling Earth Systems*, *6*(2), 441–478. https://doi.org/10.1002/2013MS000266

Ming, Y., Ramaswamy, V., Donner, L. J., & Phillips, V. T. (2006). A new parameterization of cloud droplet activation applicable to general circulation models. *Journal of the Atmospheric Sciences*, *63*(4), 1348–1356. https://doi.org/10.1175/JAS3686.1

Moritz, R. E., Bitz, C. M., & Steig, E. J. (2002). Dynamics of recent climate change in the Arctic. *Science*, *297*(5586), 1497–1502. https://doi.org/10.1126/science.1076522

Morrison, H., & Gettelman, A. (2008). A new two-moment bulk stratiform cloud microphysics scheme in the Community Atmosphere Model, version 3 (CAM3). Part I: Description and numerical tests. *Journal of Climate*, *21*(15), 3642–3659. https://doi.org/10.1175/2008JCLI2105.1

Myhre, G., Shindell, D., Bréon, F.-M., Collins, W., Fuglestvedt, J., Huang, J., et al. (2013). Anthropogenic and Natural Radiative Forcing. In T. F. Stocker, et al. (Eds), *Climate Change 2013: The Physical Science Basis. Contribution of Working Group I to the Fifth Assessment Report of the Intergovernmental Panel on Climate Change* (pp. 659–740). Cambridge, United Kingdom and New York: Cambridge University Press.

Naik, V., Horowitz, L. W., Fiore, A. M., Ginoux, P., Mao, J., Aghedo, A. M., & Levy, H. (2013). Impact of preindustrial to present-day changes in short-lived pollutant emissions on atmospheric composition and climate forcing. *Journal of Geophysical Research: Atmospheres*, *118*, 8086–8110. https://doi.org/10.1002/jgrd.50608

Neale, R. B., Chen, C. C., Gettelman, A., Lauritzen, P. H., Park, S., Williamson, D. L., et al. (2012). Description of the NCAR community atmosphere model (CAM 5.0). NCAR Tech. Note NCAR/TN-486+ STR.

Otto-Bliesner, B. L., Brady, E. C., Fasullo, J., Jahn, A., Landrum, L., Stevenson, S., et al. (2016). Climate variability and change since 850 CE: An ensemble approach with the community Earth system model. *Bulletin of the American Meteorological Society*, *97*(5), 735–754. https://doi.org/10.1175/BAMS-D-14-00233.1

Paulot, F., Fan, S., & Horowitz, L. W. (2016). Contrasting seasonal responses of sulfate aerosols to declining SO_2 emissions in the Eastern US: Implications for the efficacy of SO_2 emission controls. *Geophysical Research Letters*, *44*, 455–464. https://doi.org/10.1002/2016GL070695

Preisendorfer, R. W., & Mobley, C. D. (1988). *Principal component analysis in meteorology and oceanography* (Vol. 17). Amsterdam: Elsevier Science Ltd.

Rasmussen, D. J., Fiore, A. M., Naik, V., Horowitz, L. W., McGinnis, S. J., & Schultz, M. G. (2012). Surface ozone-temperature relationships in the eastern US: A monthly climatology for evaluating chemistry-climate models. *Atmospheric Environment*, *47*, 142–153. https://doi.org/10.1016/j.atmosenv.2011.11.021

Rotstayn, L. D., Plymin, E. L., Collier, M. A., Boucher, O., Dufresne, J. L., Luo, J. J., et al. (2014). Declining aerosols in CMIP5 projections: Effects on atmospheric temperature structure and midlatitude jets. *Journal of Climate*, *27*(18), 6960–6977. https://doi.org/10.1175/JCLI-D-14-00258.1

Russell, G. L., Miller, J. R., & Rind, D. (1995). A coupled atmosphere-ocean model for transient climate change studies. *Atmosphere-Ocean*, *33*(4), 683–730. https://doi.org/10.1080/07055900.1995.9649550

Schmidt, G. A., Kelley, M., Nazarenko, L., Ruedy, R., Russell, G. L., Aleinov, I., et al. (2014). Configuration and assessment of the GISS ModelE2 contributions to the CMIP5 archive. *Journal of Advances in Modeling Earth Systems*, *6*(1), 141–184. https://doi.org/10.1002/2013MS000265

Schmidt, G. A., Ruedy, R., Hansen, J. E., Aleinov, I., Bell, N., Bauer, M., et al. (2006). Present-day atmospheric simulations using GISS ModelE: Comparison to in situ, satellite, and reanalysis data. *Journal of Climate*, *19*(2), 153–192. https://doi.org/10.1175/JCLI3612.1

Schwarzkopf, M. D., & Ramaswamy, V. (1999). Radiative effects of CH4, N2O, halocarbons and the foreign-broadened H2O continuum: A GCM experiment. *Journal of Geophysical Research*, *104*, 9467–9488. https://doi.org/10.1029/1999JD900003

Shindell, D. (2007). Local and remote contributions to Arctic warming. *Geophysical Research Letters*, *34*, L14704. https://doi.org/10.1029/2007GL030221

Shindell, D., & Faluvegi, G. (2009). Climate response to regional radiative forcing during the twentieth century. *Nature Geoscience*, *2*(4), 294–300. https://doi.org/10.1038/ngeo473

Shindell, D. T. (2012). Evaluation of the absolute regional temperature potential. *Atmospheric Chemistry and Physics*, *12*(17), 7955–7960. https://doi.org/10.5194/acp-12-7955-2012

Shindell, D. T., Faluvegi, G., Rotstayn, L., & Milly, G. (2015). Spatial patterns of radiative forcing and surface temperature response. *Journal of Geophysical Research: Atmospheres*, *120*, 5385–5403. https://doi.org/10.1002/2014JD022752

Shindell, D. T., Lamarque, J. F., Schulz, M., Flanner, M., Jiao, C., Chin, M., et al. (2013). Radiative forcing in the ACCMIP historical and future climate simulations. *Atmospheric Chemistry and Physics*, *13*(6), 2939–2974. https://doi.org/10.5194/acp-13-2939-2013

Shindell, D. T., Pechony, O., Voulgarakis, A., Faluvegi, G., Nazarenko, L., Lamarque, J. F., et al. (2013). Interactive ozone and methane chemistry in GISS-E2 historical and future climate simulations. *Atmospheric Chemistry and Physics*, *13*(5), 2653–2689. https://doi.org/10.5194/acp-13-2653-2013

Shindell, D. T. (2014). Inhomogeneous forcing and transient climate sensitivity. *Nature Climate Change*, *4*(4), 274–277. https://doi.org/10.1038/nclimate2136

Smith, R. A. (1872). Air and rain: The beginnings of a chemical climatology. Longmans, Green, and Company.

Smith, S. J., Aardenne, J. V., Klimont, Z., Andres, R. J., Volke, A., & Delgado Arias, S. (2011). Anthropogenic sulfur dioxide emissions: 1850–2005. *Atmospheric Chemistry and Physics*, *11*(3), 1101–1116. https://doi.org/10.5194/acp-11-1101-2011

Stjern, C. W., Samset, B. H., Myhre, G., Bian, H., Chin, M., Davila, Y., et al. (2016). Global and regional radiative forcing from 20% reductions in BC, OC and SO 4–an HTAP2 multi-model study. *Atmospheric Chemistry and Physics*, *16*(21), 13,579–13,599. https://doi.org/10.5194/acp-16-13579-2016

Stott, P. A., Gillett, N. P., Hegerl, G. C., Karoly, D. J., Stone, D. A., Zhang, X., & Zwiers, F. (2010). Detection and attribution of climate change: A regional perspective. *Wiley Interdisciplinary Reviews: Climate Change*, *1*(2), 192–211.

Tebaldi, C., & Knutti, R. (2007). The use of the multi-model ensemble in probabilistic climate projections. *Philosophical Transactions of the Royal Society of London A: Mathematical, Physical and Engineering Sciences*, *365*(1857), 2053–2075. https://doi.org/10.1098/rsta.2007.2076

Tilmes, S., Lamarque, J. F., Emmons, L. K., Kinnison, D. E., Ma, P. L., Liu, X., et al. (2015). Description and evaluation of tropospheric chemistry and aerosols in the Community Earth System Model (CESM1. 2). *Geoscientific Model Development*, *8*(5), 1395–1426. https://doi.org/10.5194/gmd-8-1395-2015

Voigt, A., Pincus, R., Stevens, B., Bony, S., Boucher, O., Bellouin, N., et al. (2017). Fast and slow shifts of the zonal-mean intertropical convergence zone in response to an idealized anthropogenic aerosol. *Journal of Advances in Modeling Earth Systems*, *9*(2), 870–892. https://doi.org/10.1002/2016MS000902

Westervelt, D. M., Conley, A. J., Fiore, A. M., Lamarque, J.-F., Shindell, D., Previdi, M., et al. (2017). Multimodel precipitation responses to removal of U.S. sulfur dioxide emissions. *Journal of Geophysical Research: Atmospheres*, *122*, 5024–5038. https://doi.org/10.1002/2017JD026756

Winton, M., Adcroft, A., Griffies, S. M., Hallberg, R. W., Horowitz, L. W., & Stouffer, R. J. (2013). Influence of ocean and atmosphere components on simulated climate sensitivities. *Journal of Climate*, *26*(1), 231–245. https://doi.org/10.1175/JCLI-D-12-00121.1

Zwiers, F. W., & von Storch, H. (1995). Taking serial correlation into account in tests of the mean. *Journal of Climate*, *8*(2), 336–351. https://doi.org/10.1175/1520-0442(1995)008%3C0336:TSCIAI%3E2.0.CO;2